AD-A286 557

REPORT DOCUMENTATION PAGE Dist. A

Form Approved
OMB No. 0704-0188

1. AGENCY USE ONLY (Leave blank)	2. REPORT DATE	3. REPORT TYPE AND DATES COVERED
	October 27, 1994	Final Report 1 Sept 91 - 31 Aug 1994

4. TITLE AND SUBTITLE

High Contrast Organic Crystal Optical Modulator For Phased Array Antenna and Optical Signal Processing

5. FUNDING NUMBERS

61101E
8146/08

6. AUTHOR(S)

K.R. Stewart
E.P. Boden
C.P. Yakymyshyn
W.T. Lotshaw

7. PERFORMING ORGANIZATION NAME(S) AND ADDRESS(ES)

General Electric Co.
P.O. Box 8
Schenectady, NY
12301-0008

Molecular OptoElectronics Corp.
Rensselaer Watervliet Facility
877 25th Street
Watervliet, NY 12189

8. PERFORMING ORGANIZATION REPORT NUMBER

AFOSR-TR- 94 0749

9. SPONSORING/MONITORING AGENCY NAME(S) AND ADDRESS(ES)

AFOSR/~~NC~~ NL
Building 410
Bolling AFB, DC 20332-6448
Dr Lee

10. SPONSORING/MONITORING AGENCY REPORT NUMBER

F4962-91-C-0075

55P 94-35909

11. SUPPLEMENTARY NOTES

12a. DISTRIBUTION/AVAILABILITY STATEMENT

Approved for public release

12b. DISTRIBUTION

A

13. ABSTRACT (Maximum 200 words)

The utility of organic salts related to 4-Dimethylamino-N-methyl Stilbazolium Tosylate, DAST, to display very useful optoelectronic properties has been broadly investigated and continues to yield new information. New materials have been developed having improved optical and physical properties. Methods for crystal growth and handling have been developed which allow the design and fabrication of useful optoelectronic devices. Design and fabrication of a linear array of high performance Fabry-Perot etalons is described.

14. SUBJECT TERMS		15. NUMBER OF PAGES
DAST	Fabry-Perot etalon	54
Optical Modulator	Organic NLO Materials	16. PRICE CODE

17. SECURITY CLASSIFICATION OF REPORT	18. SECURITY CLASSIFICATION OF THIS PAGE	19. SECURITY CLASSIFICATION OF ABSTRACT	20. LIMITATION OF ABSTRACT
Unclassified	Unclassified	Unclassified	

NSN 7540-01-280-5500

Standard Form 298 (Rev. 2-89)
Prescribed by ANSI Std. 239-18
298-102

REF 9

MOEC

HIGH CONTRAST ORGANIC CRYSTAL OPTICAL MODULATOR FOR PHASED ARRAY ANTENNA AND OPTICAL SIGNAL PROCESSING APPLICATIONS

Final Report (September 1, 1991 - August 31, 1994)
Work Performed Under Contract F49620-91-C-0075

Prepared for:

AIR FORCE OFFICE OF SCIENTIFIC RESEARCH
Bolling Air Force Base
Washington, DC 20322

Sponsored by:

Defense Advanced Research Projects Agency
DARPA Order No. 8146
Monitored By AFOSR under Contract No. F49620-91-C-0075

Submitted by:

Kevin R. Stewart
Molecular OptoElectronics Corporation
Rensselaer Watervliet Facility
877 25th Street
Watervliet, NY 12189

on behalf of:

GE Research and Devleopment Center
P.O. Box 8
Schenectady, NY 12301-0008

October 1994

The views and conclusions contained in this document are those of the authors and should not be interpreted as necessarily representing the official policies or endorsements, either expressed or implied, of the Defense Advanced Research Projects Agency or the U.S. Government

Table of Contents

Introduction:

To fully exploit the high-speed parallel information processing capabilities of optical architectures, spatial light modulators (SLM s) with improved response speed, high contrast ratio and grey-scale capability are required. Fundamentally, SLM device performance is limited by the performance of the switching materials. Currently, SLM devices using liquid crystal materials are available as large arrays with moderate resolution *but are quite slow (e.g. 30 Hz framing rates).* Research in the past few years has focused on making SLMs based on GaAlAs multiquantum-well materials. These materials operate as optical switches. While recent work has shown that large arrays can be made (e.g. 1000 x 1000 SEED arrays) *the contrast ratio of each switching element is only 10:1,* which is not sufficient for most systems applications.

Electro-optic modulators based on the Pockels effect can exhibit extremely high contrast ratios (10,000:1) and fast (GHz) switching. However pixels based on such modulators, which could be made into arrays for SLMs, have not been achieved. *Conventional electro-optic materials such as lithium niobate do not possess sufficient electro-optic figures of merit to allow the demonstration of such arrays.* With tolerable drive-power requirements, such modulators cannot exhibit high-contrast ratios.

A multi-pixel array SLM which exhibits a greater than one hundred to one contrast ratio, a low insertion loss, and a switching voltage of less than 100 volts at GHz modulation speeds, would represent a significant breakthrough in SLM performance.

During the course of the investigations which are being described in this report, we have studied a series of 4-substituted-N-methyl stilbazolium salts and have shown that these materials are extremely promising candidates for fabricating a fast (>1 GHz framing rate), high-contrast (>100:1) SLM that operates using voltages accessible with integrated circuit technology. In a three year program, we have investigated new and existing organic materials and discovered that these organic salts are suitable for the fabrication of optical modulators exhibiting a greater than 100:1 contrast ratio, with a switching voltage of less than one hundred volts. Four areas of investigation were required to achieve this goal: (1) Enhancing the molecular nonlinearity of materials by engineering the molecular shape, dipole strength and polarizability of chromophores. (2) Development of high-yield scalable synthetic routes which provide high purity starting materials for single crystal growth. (3) Fabrication of single crystal materials. (4) Design, fabrication and testing of prototype modulators using optimized modulator geometries.

This report describes a series of investigations that were originally started at the GE Corporate Research & Development Center in late 1991 and continued there until August of 1993 when GE turned the technology over to Molecular OptoElectronics Corporation (MOEC), a company with a mission to commercialize the developments on these and other optical materials, and devices fabricated from these materials.

Materials Research:

The materials research portion of this program was directed at the synthesis of new materials and at optimizing procedures for the scale-up of stilbazolium salt production; particularly of 4-Dimethyl Amino-N-methyl Stilbazolium Tosylate (DAST). As a result of these efforts, we have found a series of new materials, including one known as DASM, which offers a convenient route to a variety of other stilbazolium salts. By utilizing this material, we have carried out a series of ion exchange reactions to obtain an extensive set of related salts which were examined for NLO active crystalline phases.

Preparation of 4-Dimethyl Amino-N-methyl Stilbazolium Mesylate (DASM):

A new stilbazolium salt has been prepared in which the counterion is a mesylate (CH_3SO_3-) instead of a tosylate ($C_7H_7SO_3$-). This new material, refered to as DASM, has a melting point of 212 -215° C and possesses a rich morphology. Although a hydrated form of DASM actually has the highest powder SHG properties of any material yet reported, this material has more utility as a precursor for counterion exchange reactions to form new NLO materials than as a material for modulator fabrication. DASM is unusually soluble at ambient temperature in both water (> 65 g/L) and methanol (> 250 g/L). Most of the other stilbazolium salts we have tested have solubilities more like DAST, which has solubilities of 0.65 g/L in water and 25 g/l in methanol. Thus, by utilizing DASM, counterion exchange reactions can be cleanly done at reasonable concentrations in aqueous or organic media without the need for multiple crystallizations to remove the original salt from the product. A patent has been issued on the synthesis, composition of matter and applications of DASM [1]. A number of new salts have been prepared from DASM, as illustrated in the **Table 1**.

During the syntheses of the organic salts described in this report we examined many variations on the synthetic sequence in order to optimize the process for scale-up to provide bulk materials for device fabrication. The major problem turned out to be the utilization of piperidine as the amine catalyst for the condensation reaction during the synthesis. We have come under increasing pressure to stop using piperidine as a catalyst for the preparation of DAST because piperidine is a controlled chemical. Currently, piperidine must always be kept in a doubly-locked cabinet requiring two different keys for access. Using large quantities of piperidine, especially in a large scale preparation of DAST, would be particularly problematic. Thus, we investigated several other secondary amines for use in the condensation of the picoline salt with various substituted benzaldehydes.

Table 1: Effect of Counterion on Powder Efficiencies

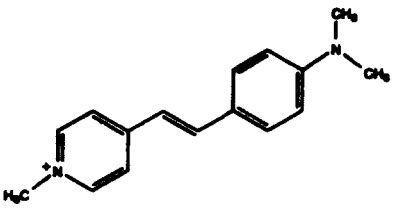

Counterion X-	Color of Crytals	SHG x Urea @ 954 nm	THG x DANS @ 636 nm	Crystal Structure
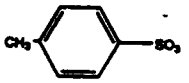	green	1000	200	Monoclinic Cc
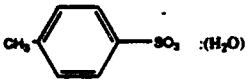	orange	0	0	Triclinic P1
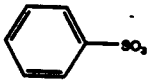	red	0	0	Triclinic P1
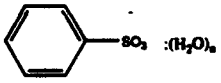	green	300	25	—
CH_3SO_4:(???)	red	700	30	—
I	purple	0	0	Triclinic P1
Cl	yellow	60	0	—
CH_3SO_3	orange	200	25	—
CH_3SO_3:$(H_20)_4$	blue/green	1200	40	Monoclinic Cc
CH_3SO_3:$(H_20)_{<4}$	purple	50	2	—
CH_3SO_3	red	0	0.5	Monoclinic $P2_1/c$
PF_6	red	0	0	—
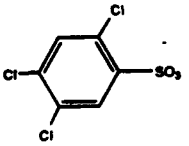	orange	0	0	—
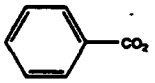	green	300	2	—

Note: Particle size variations can give ±10% errors in powder efficiencies.

Alternate Catalysts:

We have found several useful condensation catalysts which have a wide range of catalytic effects, as evidenced by the relative rates of reaction (pyrrolidine > piperidine & morpholine >> diethylamine). Pyrrolidine has proven to not only speed the reaction at concentrations similar to piperidine, but also has produced more consistent results and higher quality products. Often piperidine catalyzed reactions would not proceed properly and would require subsequent additions of catalyst to initiate the reaction. All of the pyrrolidine reactions went to completion in the same time frame for a given level of catalysts despite changes in aldehydes and reaction scale. Two-step isolated yields of DAST are typically 90% with either pyrrolidine or piperidine. This process improvement has been protected under United States and overseas patents [2].

Preparation of DAST - Scale-ups:

One objective of this contract was to demonstrate that significant quantities of DAST could be made in a single reactor, in order to show that organic nonlinear optical materials are not just of academic interest, but are also commercially viable. Initial scale-ups on 1-2 kg scale were done in 5 L reactors using piperidine as a catalyst. Isolation of the product was done by cooling the reaction mixture and filtering the DAST from the methanol solution.

Prior to a pilot plant scale-up, pyrrolidine had been identified as the catalyst of choice. Thus, a 10 gallon glass lined reactor was charged with 12 L of methanol, 3.120 kg of picoline, and 6.046 kg of methyl toluene sulfonate. The reaction mixture was gently refluxed overnight while maintaining stirring. The next morning, the solution was cooled to 20 -30° C and 4.958 kg of N,N-dimethylamino benzaldehyde was added to the newly formed picoline salt, together with an additional 6 L of methanol. Finally, 500 mL of pyrrolidine were slowly added to the reaction mixture at 55° C. There was a sudden exotherm associated with addition of the catalyst which caused some of the reaction mixture to be ejected from the vessel. The mixture refluxed for 3 hours to complete the condensation and then the reactor was externally cooled to further precipitate the product. Due to time constraints, the solution temperature was only reduced to 6-10° C instead of what is normally an extended period of time at 0-5° C. Thus, a higher than usual amount of the product remained in solution. The slurry of DAST in methanol was gravity fed from the reactor through a 2 inch glass pipe to a basket centrifuge and the crystalline product was collected.

The product was removed and dried in vacuum ovens to yield approximately 9 kg of DAST. Upon cleaning the reactor with hot methanol the next day, an additional 1.4 kg of DAST were recovered. A significant amount of product probably remained dissolved in the hot methanol and was inadvertently discarded. The final isolated yield of DAST was 10.38 kg or approximately an 80% yield. A somewhat lower than usual yield was obtained due to some first time processing problems that should be easily avoided in the future. The product was very pure and possessed a melting point of 256 -258° C, comparable with excellent quality DAST made on any other scale.

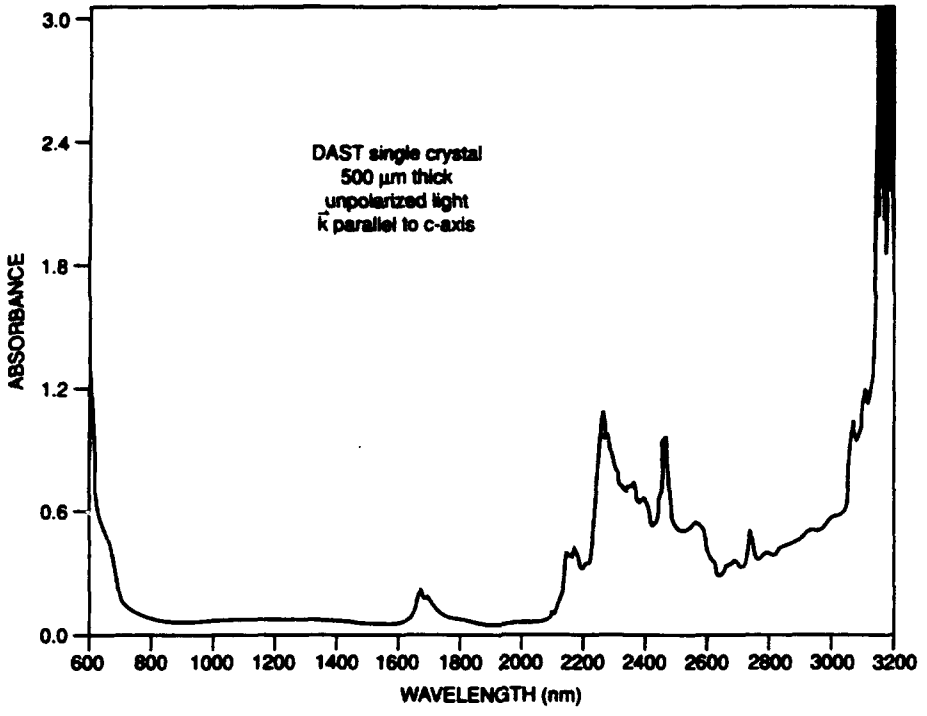

Figure 1: Absorption Spectra of DAST

Preparation of Deuterium Substituted DAST:

The 1670-2000nm region of the spectrum of aromatic compounds display several weak bands which are overtone and combination bands for the in-plane and out-of-plane bending deformations of the C-H units. In the solid state where the molecular concentration is very high, these bands are quite intense and subject to change upon substitution. It is well know that substitution of an atom by a heavier isotope, for example deuterium for hydrogen, results in a shift of the absorption band to lower frequencies. DAST and similar organic compounds being used for their unique NLO properties exhibit these bands in the 1600-1800nm region of their spectra, **Figure 1**, a region which is extremely useful for applications such as long distance optical fiber communications and eye-safe remote sensing,

It has been shown that the substitution of deuterium for hydrogen will remove the C-H overtone regions of the absorbance spectrum for aromatic organic compounds. This is a standard technique used during the assignment of the spectral modes observed for an organic compound and aids in the identification of specific C-H positions which are responsible for the specific

modes. It has also been observed in the example of potassium dihydrogen phosphate versus potassium dideuterium phosphate, that the replacement of deuterium for the hydrogens lead to a shift in the absorbance spectrum edge from 1400 nm for KH_2PO_4 to about 1800 nm for KD_2PO_4.

Prior to synthesizing these novel perdeuterated materials, a series of computer-aided materials simulations were carried out to examine the utility of specific deuterium for hydrogen substitution on the spectrum of the final product. Shown below, **Figures 2 and 3**, are illustrations of the computed infrared spectra for the normal DAST molecule and the perdeuterated DAST d-26. These spectra dramatically illustrate the reduction in the C-H stretching frequencies, normally located at approximately 3000 cm-1, when deuterium is substituted.

Fortified with this information, 4-dimethylamino N-methyl stilbazolium iodide was synthesized from perdeuterio 4-dimethylamino benzaldehyde, perdeuterio 4-picoline and perdeuterio methyl iodide. Perdeuterio p-toluene sulfonic acid was synthesized by the method of Fieser, starting with perdeuterated toluene and sulfuric acid. The two units of the structure were combined to yield perdeuterated DAST (DAS-d_{19} T-d_7) via the silver salt chemistry of Kornblum. The UV-visible spectrum of DAST-d26 crystals reveals efficient removal of the several weak bands which resulted from the overtone and combination bands for the in-plane and out-of-plane bending deformations of the C-H units in the 1670-2000nm region of the spectrum. The composition of matter and application of these deuterated materials to electro-optic devices have been covered under United States patents [3,4].

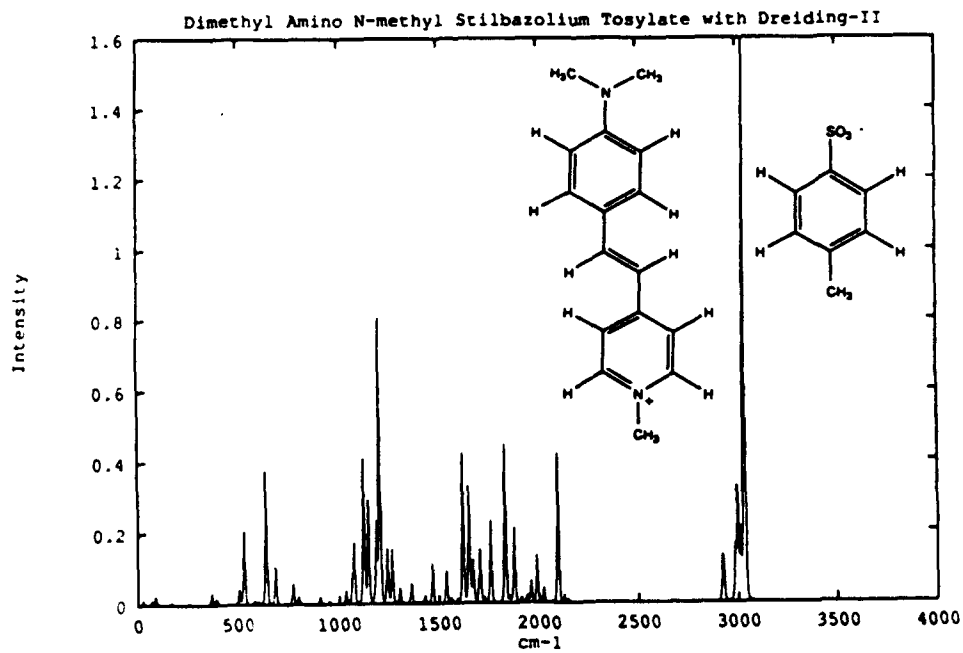

Figure 2: Computed IR spectrum for DAST

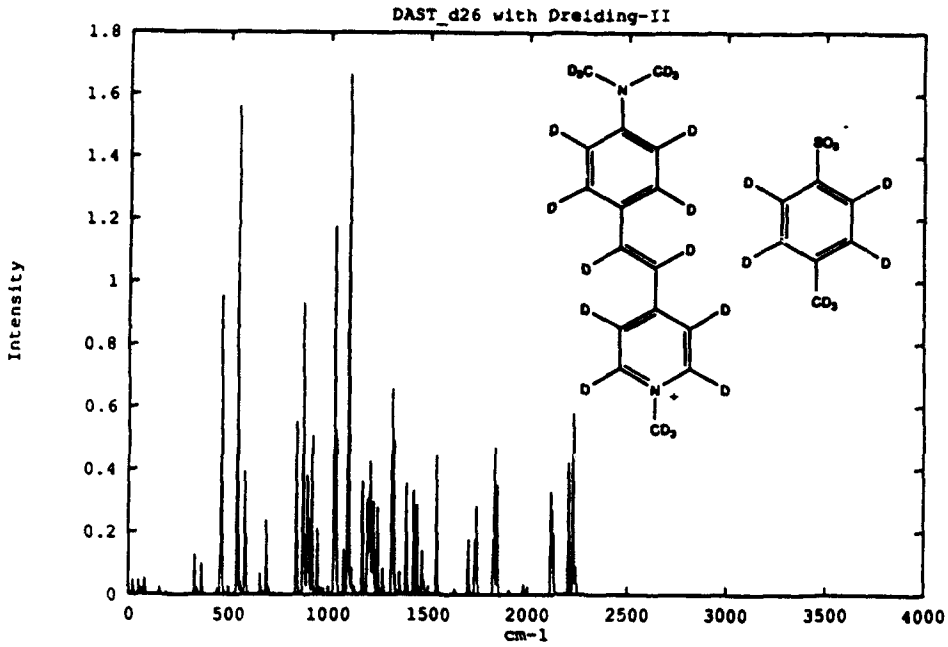

Figure 3: Computer IR spectrum for DAST d-26

Crystal growth:

Several approaches were investigated to create films or bulk crystals of organic salts. These can be divided into solution-based techniques and melt-based techniques. Solution growth was successful, and continues to provide the best crystals. We carried out selective investigations of the thin-film growth of DAST, because of enormous impact on device fabrication, if deposition of thin films can be successfully achieved.

During the course of these investigations many variables were found to effect the reproducibility of the crystal growth of DAST and other salts. We therefore designed and built a crystal growth facility specifically for growing crystals of DAST. Water concentration was determined to be important factor in growing high quality crystals. For DAST, water concentrations below a few hundred ppm in methanol are required to grow high-quality, sharp-faceted crystals. The growth facility consists of three-liter double-walled reaction vessels thermally controlled using recirculating water baths. The vessels must be carefully cleaned and dried, then filled with vacuum-dried DAST powder dissolved in methanol which has been previously distilled from magnesium turnings, yielding water concentrations of <100 ppm. Crystal growth is carried out under dry Argon. Results indicate superior crystal quality when grown under these conditions. A side effect of the low water content is a reduction in the solubility of DAST, which dropped by two-thirds when the water concentration was <100 ppm.

We have grown crystals of DAST as large as 12 x 10 x 5 mm^3 with small defects, and routinely grow high quality crystals 5 x 5 x 2 mm^3 in size. The current limitation in crystal size seems to be the relatively low solubility of DAST in dry methanol, which limits the total solution concentration available at a given growth temperature. Higher temperature growth is useful, although experience has shown poor crystal quality when grown at temperatures >40 °C.

We have also examined the growth of other organic salts. In particular, the compound 4-methoxy-N-methylstilbazolium tosylate, MOST, has been investigated with several growth solvents. Methanol has again provided the best results, although the effects of water as a co-solvent are more complex. High quality crystals of the P1 phase of MOST were grown when the methanol growth solution had several thousand ppm of water present. Lower water concentrations resulted in poor quality crystals of the $P2_1$ phase of MOST. For water concentrations of >10%, a centric (P1) hydrate of MOST grew, forming large (5 x 5 x 3 mm^3) blocky crystals with very good optical quality.

Thin Film Growth - Thermal:

We attempted to deposit DAST thin films using conventional thermal evaporation from a resistive boat. Careful control of the deposition temperature just above the melting point of DAST was required to avoid decomposition of the material. A 0.1 μm thin film was deposited onto a glass substrate over a period of 10 minutes at 5 x 10^{-6} Torr and 265 °C, ± 10 °C. The films exhibited no SHG when illuminated with 20 nsec pulses at 1.06 μm. Although the absorption coefficient was high at the absorption peak (≈40,000 cm^{-1} at 480 nm), the absorption peak was significantly blue-shifted from the 550 nm peak measured in polycrystalline layers of solution-grown DAST, which indicated either a different crystal structure (e.g. the hydrate) or decomposition of the material. Subsequent thermal curing did not result in spectral changes in the film which would be expected as the hydrate reverted back to the acentric phase. To verify the existence of DAST on the substrate, the films were dissolved off the substrate and examined with conventional NMR. The NMR peaks, although weak, indicated an absence of the stilbazole chromophore, which verified the existence of a decomposed product. In addition, the remaining DAST in the evaporation boat solidified into a black glassy material, indicating decomposition of the source material. We do not believe that conventional thermal evaporation is a promising approach for achieving thin films suitable for device fabrication.

Thin Film Growth - Solution:

Thin film growth has been reported by others using a saturated growth solution sandwiched between glass plates. This approach was attempted using methanol or hydrochloric acid (HCl) as solvents. The solution filled a 25 - 50 μm gap between glass slides through capillary action. Over several weeks at room

temperature, the solvent slowly evaporated, resulting in crystal growth. At several locations in the sandwich, single domain sheet-like crystals grew, with areas of up to 1 mm^2 . In the case of an HCl solvent, the solubility of DAST was extremely high (> 500 g/liter), and many more crystals formed. Interestingly, both the expected hydrate of DAST [5], and the acentric anhydrous phase of DAST, were formed when growth proceeded over several months at room temperature. The resulting crystals were free-standing, and extremely fragile. In fact, removal of the crystals from the growth medium was impossible. We do not believe this is a promising approach for achieving thin films suitable for device fabrication.

An alternative to this approach involved spin-casting a supersaturated solution of DAST in HCl onto a glass substrate. The glassy layer was then cured at elevated temperatures for several hours. During cure, DAST crystallized out of solution as HCl escaped from the surface. Depending on the curing cycle, three phases of DAST could be crystallized uniformly over the substrate surface as a polycrystalline film. As the temperature was increased from 100 - 150 °C, the resulting crystalline phase changed from the orange hydrate, to a yellow hydrate, and finally to the anhydrous green phase. It was hoped that a further thermal anneal could encourage the regrowth of these crystallites into each other, forming a continuous film of interlocked crystallites. Unfortunately, no regrowth was observed at thermal annealing temperatures ranging from 150 °C to 225 °C. We do not believe this is a promising approach for achieving thin films suitable for device fabrication.

Thin Film Growth - Laser Ablative Deposition:

Thin film deposition of DAST was attempted using laser ablative deposition. This technique has been successfully used to deposit stoichiometric compositions of complex ceramics such as high temperature copper oxide superconducting films. We felt that the maintenance of stoichiometry could be used to preserve the salt structure of DAST during the deposition process. Both 248 nm excimer laser pulses and 532 nm frequency doubled laser pulses from a Q-switched Nd:YAG laser were used to ablate DAST from a single crystal source in a large vacuum chamber pumped down to 10^{-6} Torr. Pulse repetition rates of 10-100 Hz were used at a variety of pulse energies. Usually, the pulse energy was adjusted until a plume of material was observed being ejected from the surface of the DAST source. A glass substrate was mounted directly in the path of the emitted plume. Films 0.1 - 0.5 microns thick were typically deposited in 20-30 minutes. After deposition, the substrates were removed from the chamber and UV-vis absorption spectra were taken.

For all of the deposited films using the 532 nm laser, the absorption peak dominant in the visible band was centered at 450 nm, and was very broad, extending over 150 nm . The films deposited using the 248 nm excimer laser source showed an absorption peak near 400 nm. Both of these absorption peaks are blue-shifted relative to the 540 nm absorption peak of single crystal solution-grown DAST, indicating molecular decomposition of the parent stilbazolium

moiety. The films were also tested for second harmonic activity using a pulsed 1.06 micron Nd:YAG laser. No SHG activity was observed in the deposited films. To confirm the decomposition of DAST, a solution NMR was taken by dissolving several deposited films into dry DMSO. Although the NMR signals were extremely weak due to the dilute nature of the sample, there were clear indications of decomposition products and no indication of intact stilbazolium chromophores. From these results and previous unsuccessful attempts at thermal vacuum deposition of DAST, we have concluded that DAST cannot be thermally deposited using conventional vacuum evaporation or laser-ablation induced deposition processes. In addition, the 248 nm excimer pulsed source appears to be more effective at dissociating the Stilbazolium chromophore than the 532 nm pulsed laser beam.

Attempted Bridgeman Growth:

Finally, we carried out examination of the Bridgeman growth technique, using a laboratory scale zone refining apparatus. This device was designed to grow the solid inside a quartz tube having an inside diameter of 1 cm by repetatively scanning a pair of ovens over the length of the sample. Limited successes were demonstrated, but we encountered great dificulties in accurately controlling the temperature of the ovens such that decomposition of the DAST could be minimized. This method does warrant future investigation.

Crystal Structure and Crystal Morphology

During these investigations we have examined the crystal structure motif and morphology for many of the organic salts described. The variability in the crystal structure motif can lead to broad differences in the electro-optic utility of the different crystalline phases of the same organic compound. Additionally, crystal morphology can lead to bulk materials which are difficult or even impossible to fabricate into useful devices, while at the same time demonstrating extremely useful electro-optic coefficients.

DAST is a particularly good example material to illustrate these compatibilities. The crystal structure of DAST is shown in **Figure 4**. As illustrated, the molecular chromophores (DAS+ cations) responsible for the large electro-optic coefficient, allign in two dimensional sheets which are separated by sheets of the Tosylate counterions.

It has been suggested that the tendency for flat molecules to stack, coupled with strong coulombic interactions would overwhelm the deleterous dipole-dipole interactions and thereby remove the net force which leads to centrosymmetric crystallization.[6] p-Toluene sulfonate salts of 4-substituted-N-methylstilbazolium cations exhibit a particularly high incidence of noncentrosymmetric crystal packing.

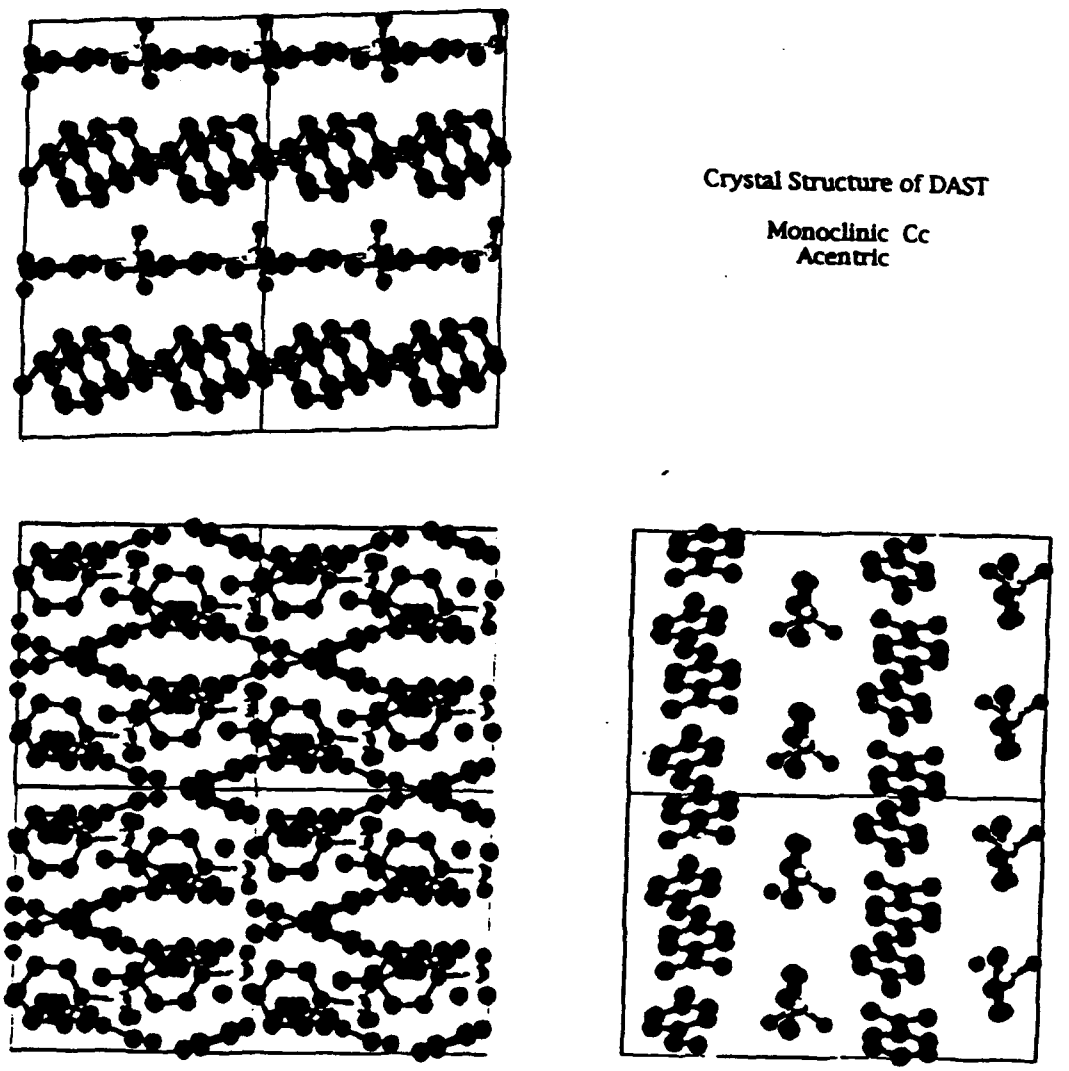

Figure 4: Crystal Structure of DAST; Views of Three Principal Axes.

Single crystal X-ray studies of DAST reveal that the large face of the Cc phase crystals contains the *ab* plane of the crystal structure, with the *a* and *b* axes along the crystal diagonals. DAST is therfore a positive biaxial crystal as represented by **Figure 5**.

$$\begin{bmatrix} d_{11} & d_{12} & d_{13} & 0 & d_{15} & 0 \\ 0 & 0 & 0 & d_{24} & 0 & d_{26} \\ d_{31} & d_{32} & d_{33} & 0 & d_{35} & 0 \end{bmatrix}$$

$$\begin{bmatrix} r_{11} & 0 & r_{13} \\ r_{21} & 0 & r_{23} \\ r_{31} & 0 & r_{33} \\ 0 & r_{42} & 0 \\ r_{51} & 0 & r_{53} \\ 0 & r_{62} & 0 \end{bmatrix}$$

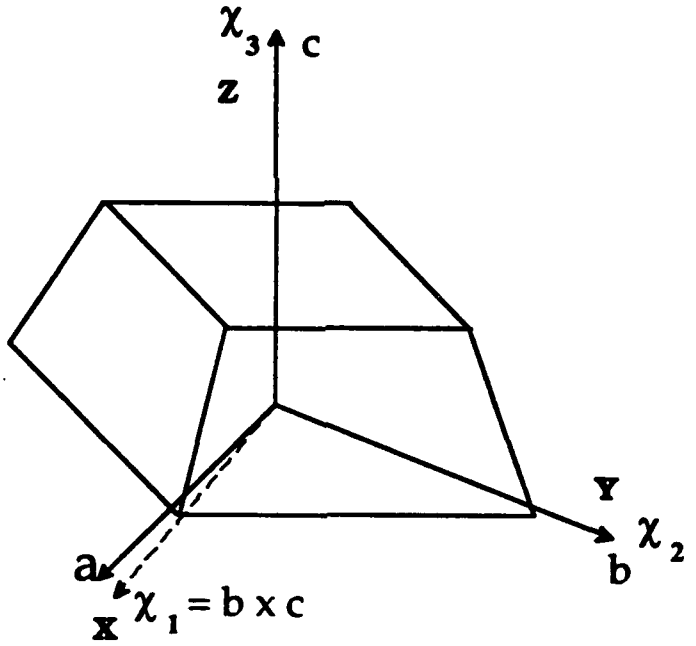

Positive Biaxial Crystal
n(x) > n(y) > n(z)

Figure 5: DAST Cc Phase Single Crystal Morphology

Characterization of Materials

Ti:Sapphire Laser System and Femtosecond Spectroscopy:

During the course of these studies we designed and built a synchronously pumped, hybridly modelocked Ti:Sapphire oscillator for femtosecond time-resolved spectroscopy, as shown in **Figure 6**. The pump laser is a cw-modelocked Nd:YAG laser (Spectron Laser Systems, Ltd.) which delivers 5W of average power at the 532nm second harmonic. The Ti:Sapphire oscillator depicted in the figure consists of a 1 cm Ti:Sapphire crystal (specific absorption @ 532nm = 2.8 cm-1, Crystal Systems, Inc.), a flat high reflector (HR), 2 Schott F2 glass Brewster prisms (P1,P2), a dichroic mirror through which pump radiation at 532 nm is delivered (R=100% @ 800nm, R less than or equal to 3% @ 532nm), two curved folding mirrors (R1, R2 with radius of curvature = 10 cm), and a flat partially transmitting output coupler (Rout). We have observed average power output of up to 1W, with 50 fs pulse durations and excellent peak-peak stability (less than 2% p-p). Pulse duration is controlled by the variation of optical path length in prism P1.

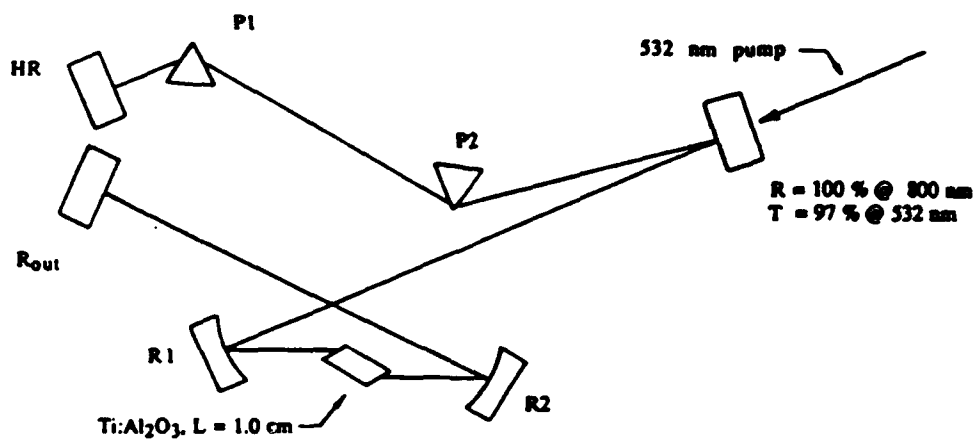

Figure 6: Ti:Sapphire Laser System

Some of the principal limitations of materials for electro-optic and photonic device applications can be traced to the distribution of the nonlinear optical susceptibility among pure electronic and vibrational origins. The distribution may be interrogated conveniently in the femtosecond time domain

as indicated in **Figure 7**. The broad laser pulse bandwidth can be used to construct the optical cross-sections of the complex nonlinear susceptibility X^3 via time resolved four wave mixing.

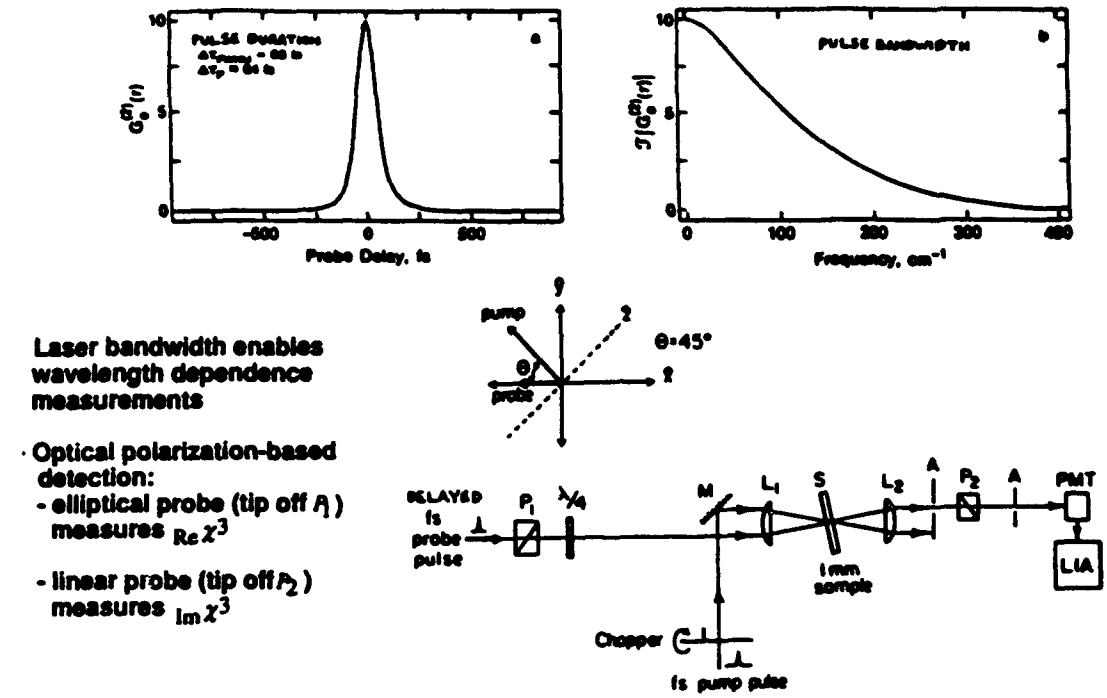

Figure 7: Optical Heterodyne Detected Femtosecond Four Wave Mixing.

The laser pulse is passively divided by a beam splitter into a strong pump pulse and a variably delayed weak probe pulse. The pump pulse creates a nonlinear polarization in the material that is probed at various times prior to and following the passage of the pump pulse through the material. In this way the transient nonlinear optical response of the material is discretely sampled at many equally spaced time intervals within a range of several tens of picoseconds. This data may then be analyzed via fast Fourier transform techniques to obtain the effective nonlinear optical susceptibility of the material within the laser bandwidth. This approach exhibits dramatically improved signal to noise and low frequency resolution in the vibrational frequency range of 10 GHz to 10 THz due to the polarization based detection scheme, which is nearly background free (unlike conventional CARS or spontaneous Raman spectroscopy).

DAST crystals (Cc phase) have been interrogated by transient four wave mixing in the optical Kerr geometry (2 beams; ellipse rotation of a weak probe beam induced by a noncollinear pump beam). These experiments are designed to measure the magnitude of X^3 relative to a standard reference material (carbon disulfide) and detect the distinct contributions of electronic and vibrational processes to X^3. At 810 nanometers, using 40 femtosecond pulses derived from a modelocked Ti:Sapphire laser, the X^3 of DAST measured along the *a, b* axes of

the crystal, is on the order of 50-100 times smaller that of carbon disulfide. The X^3 is dominated by electronic processes which are weakly modulated by Raman modes of the material. During the present measurements, 2-photon absorption, harmonic generation, and optical rectification, will effect the results.

Single crystal plates of the acentric DAST Cc phase, the centric P1 phase of DAST hydrate, and methanolic solutions of DAST and the methoxy analog MOST, have been interrogated by femtosecond time-resolved four-wave mixing spectroscopy. The Raman induced Kerr effect (RIKE) measures the anisotropy of the third order optical nonlinearity X^3, that is, linear combinations of the off-diagonal tensor elements. In the solid samples, the molecular nonlinearities can be strongly modulated by the crystal lattice, resulting in substantially altered bulk (device relevant) properties. The goal of the femtosecond RIKE studies was to examine the magnitude of X^3 and the effects arising from the lattice structure and dynamics.

At 810 nm, using 40 femtosecond pulses derived from a modelocked Ti:Sapphire laser, the X^3 of the DAST Cc phase was measured in the *ab* plane.

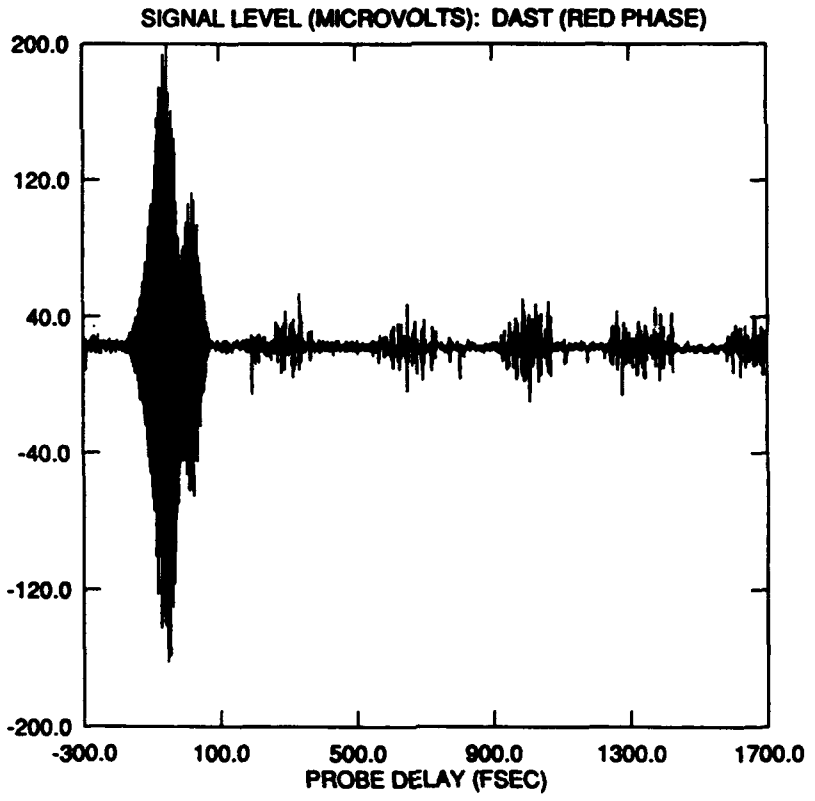

Figure 8: RIKE spectra of DAST Cc Phase Single Crystal

The X^3 of the sub-millimeter thick plate was 50-100 times smaller than that of a carbon disulfide reference. The measured transient shows several unexpected features: (1.) recurrences ('echoes') in the RIKE signal with variable periods, (2.) fine structure in the response envelope corresponding to the 2.7 fs period of the laser frequency. Neither the recurrences ('echoes'), nor the signal oscillations at the optical frequency of the laser are expected in the 2-beam, pump-probe geometry of the RIKE experiment. Several of the unique properties of the DAST stilbazolium chromophore and crystal structure may be relevant to the explanation of these features. Among these is that the chromophores and the crystals are strong two-photon absorbers at the wavelengths used. A preliminary portion of this work was presented at the OSA conference on organic thin films in Toronto on October 7, 1993.

Maker Fringe Measurements

Figure 9 shows the early Maker Fringe experiment assembled to measure the second-order nonlinear optical d coefficients of crystals. A Q-switched Nd:YAG laser generating up to 500 mJ pulses at 1.06 μm was weakly focused into a high-pressure (400 - 600 psi) hydrogen cell. The Raman-scattered light was spectrally separated by a Pellin-Broca prism, such that only the first Stokes-shifted signal at 1.905 μm continued to the sample crystal. A computer-controlled one-axis rotation stage was used to vary the incident angle of the 1.905 μm beam relative to the crystal surface. As-grown samples of DAST single crystals were rotated while monitoring the second harmonic optical signal with a photodetector having appropriate optical filters. The detected second harmonic signal was normalized to the second-harmonic signal generated by a powder sample of Urea, which reduced the noise caused by pulse-to-pulse fluctuations in the laser pulsewidth and amplitude. A typical data set is shown in **Figure 10**, where the d_{11} coefficient of DAST has been measured relative to the d_{33} coefficient of lithium niobate. The adjacent minima in this figure give a coherence length of $L_{11} = 2.4$ μm, and with d_{33} ($LiNbO_3$) = 30 pm/V, the resulting coefficient for DAST is $d_{11} \approx 500$ pm/V, ± 100 pm/V. Resonance contributions to this very large nonlinearity are small, because of the spectral distance between the second harmonic signal at 954 nm and the dominant one-photon absorption peak centered at 540 nm. In a similar manner, d_{12} (DAST) = 220 pm/V ±50 pm/V, and $L_{12} \approx 1.7$ μm. Brian Lawrence received a master's thesis at MIT (1992) based on these measurements, and is currently a graduate student with Professor George Stegeman at CREOL, University of Central Florida.

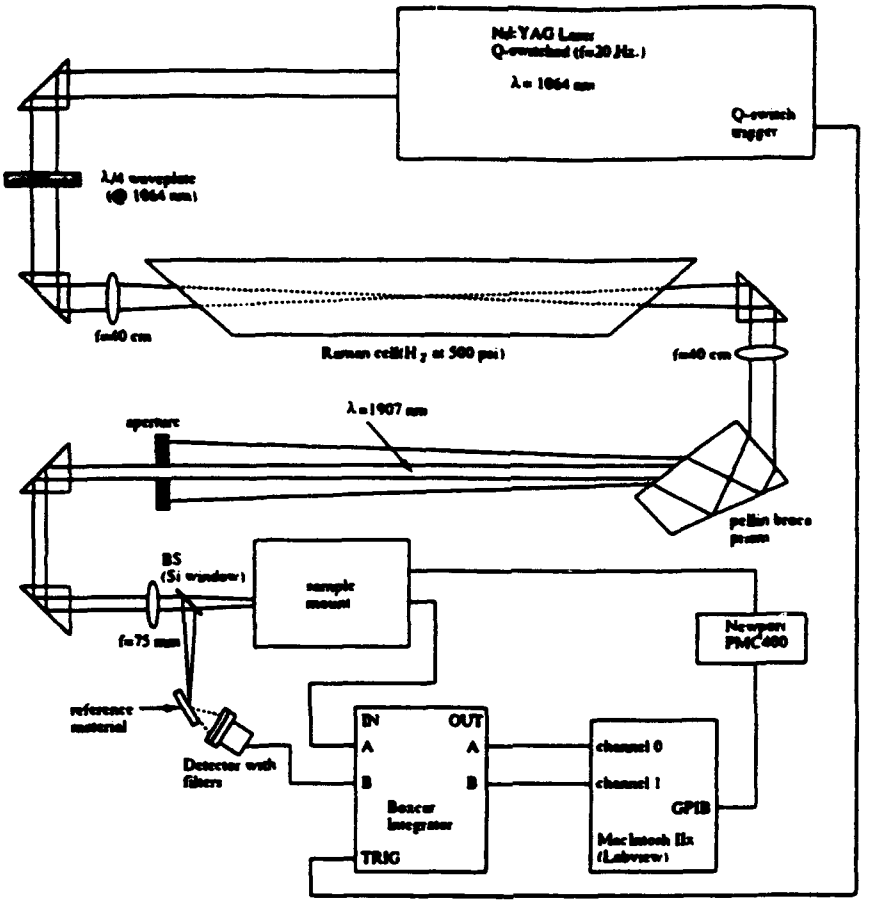

Figure 9: Optics Setup for Maker Fringe Measurements.

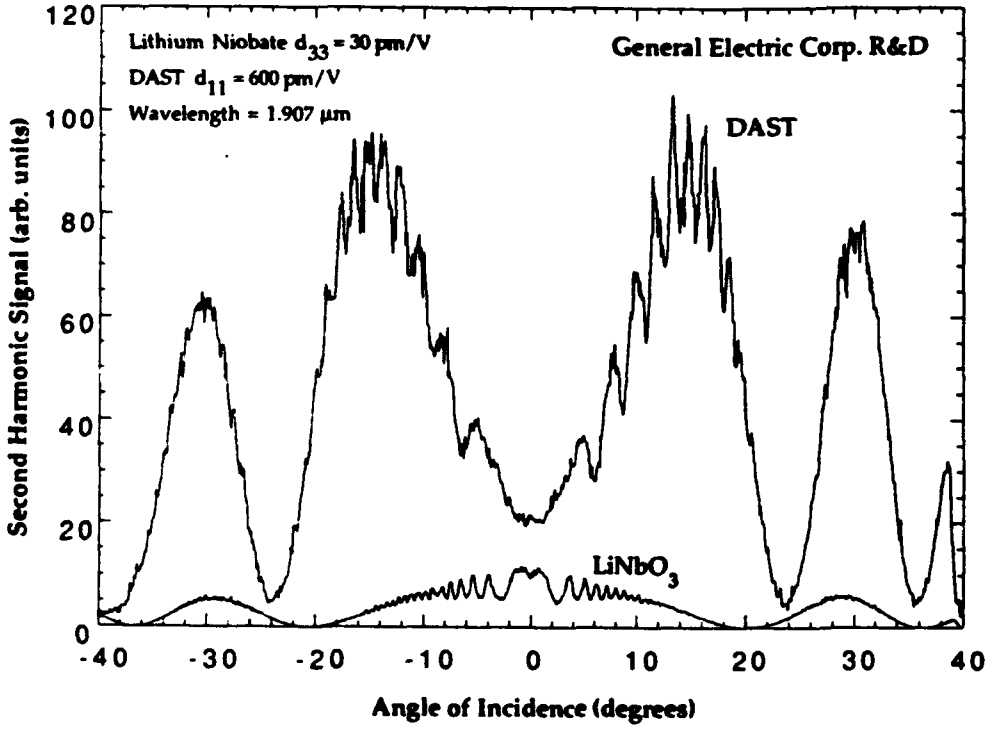

Figure 10: Maker Fringe Data on DAST.

To investigate the resonance enhancement of the nonlinearity in DAST and other materials, an optical parametric oscillator (OPO) was assembled, as illustrated in **Figure 11**, using KTP as the nonlinear crystal. A Q-switched Nd:YAG laser generating 25 mJ pulses at 532 nm was coupled into a plano-plano optical cavity containing a 10 mm long KTP crystal cut for phase-matched optical parametric generation tunable from 1.2 - 2 μm in the idler beam, and 0.72 - 0.95 μm in the signal beam. A tuning curve of the idler output is shown in **Figure 12**. Continuous tuning from 1.2 - 2.0 μm was achieved using a single KTP crystal and two sets of near-infrared cavity mirrors, with up to 2.5 mJ of output pulse energy per beam (beams emerge from both sides of the cavity), giving an overall conversion efficiency of ≈20%. The measured optical linewidth was <2 nm, or <10 cm^{-1}, which is suitable for Maker Fringe studies. **Figure 13** shows Maker fringes of a Lithium Niobate reference sample at two wavelengths, 1.2 μm and 1.4 μm. The data in **Figure 13** were collected five times faster than data shown in **Figure 9**. The reduced data collection time, with simultaneous maintenance of an excellent signal to noise ratio, is attributed to the superior beam quality and pulse-to-pulse stability of the OPO output beam.

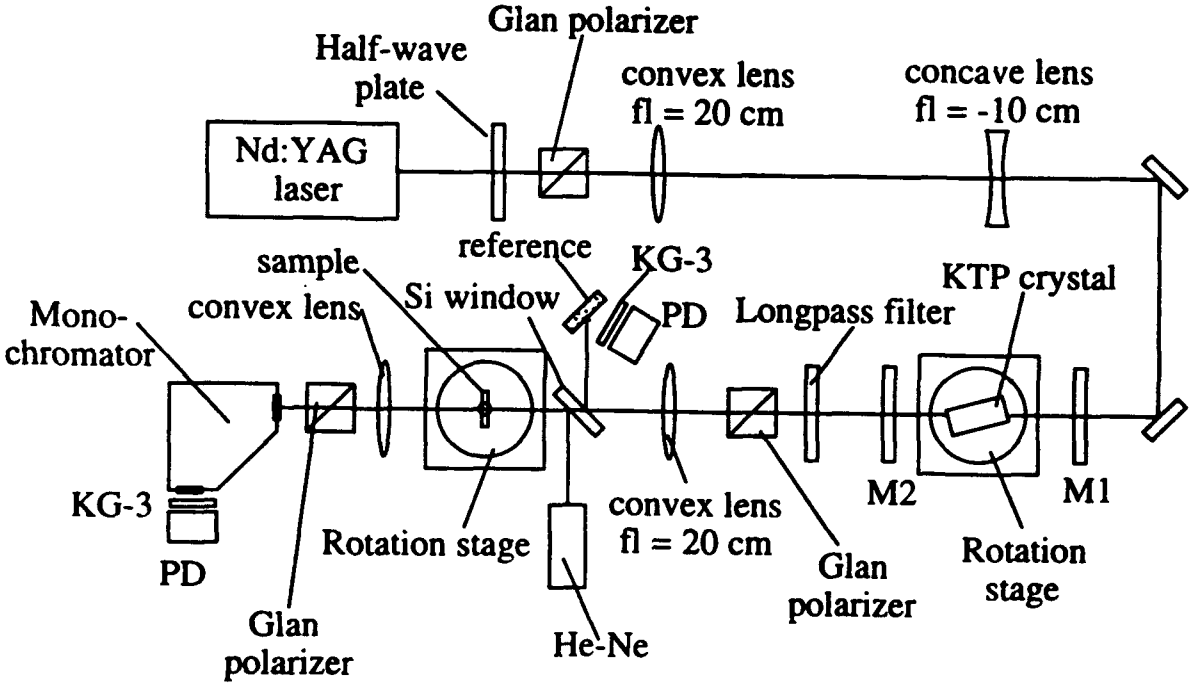

Figure 11: Optical Parametric Oscillator .

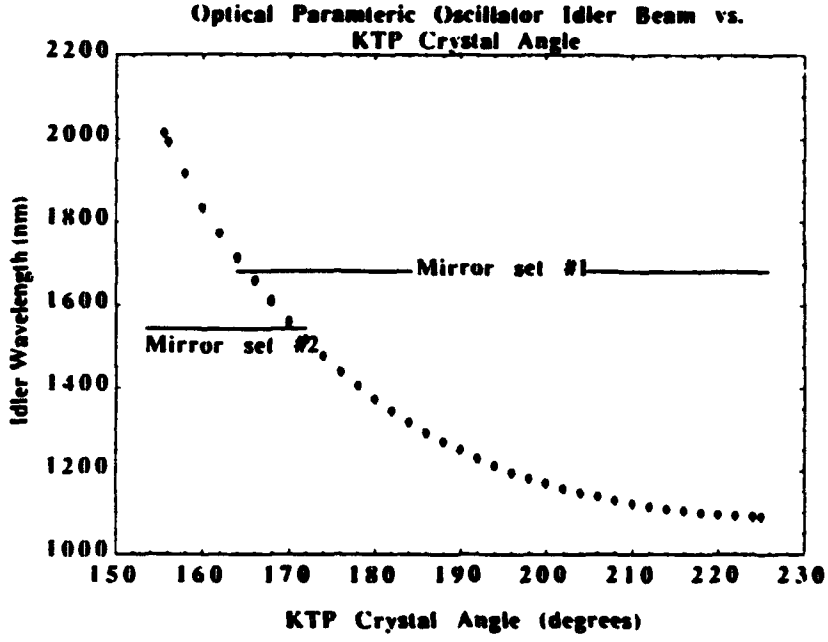

Figure 12: Optical Parametric Oscillator Idler Beam vs. KTP Crystal Angle.

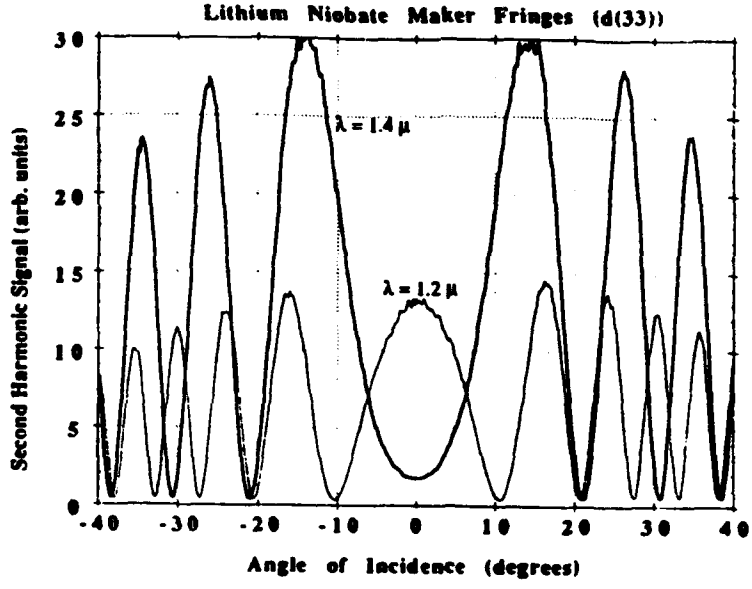

Figure 13: Maker Fringes of Lithium Niobate.

The electro-optic response of DAST crystals was investigated at high frequencies in the near-infrared spectral region to determine if vibrational contributions to the nonlinear coefficients were present. In two collaborative experiments, the electro-optic response of a DAST single crystal was measured from 1-40 GHz, and from 100 - 1000 GHz. The first experiment, shown in **Figure 14**, was performed at Stanford University by John Thackara under the supervision of Prof. David Bloom. A coplanar transmission line generated a microwave electric field near the surface of an as-grown DAST crystal. A modelocked 1.06 μm Nd:YAG laser provided a probe pulse which sampled the electric-field induced birefringence in the DAST crystal at different positions on the microwave signal. The maximum measured birefringence was then plotted as a function of the applied microwave frequency, and is shown in the bottom of **Figure 14**. The response is flat over the frequency range probed. In addition, no changes in response were seen over time, even for total optical doses of more than 10 MJ/cm^2, indicating good photochemical stability of DAST in the near infrared.

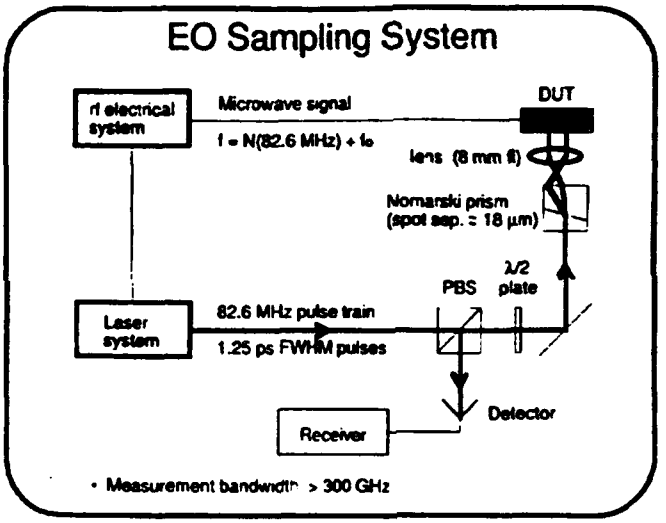

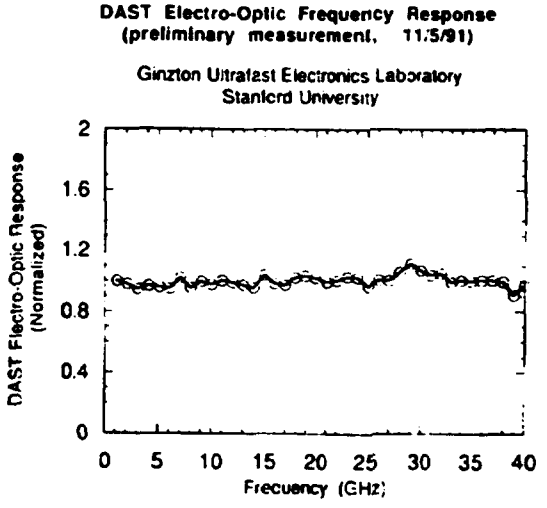

Figure 14: DAST Electro-Optic Frequency Response.

In a continuing collaboration with Prof. X. C. Zhang of Rensselaer Polytechnic Institute, a modelocked femtosecond Titanium-doped sapphire laser was used to generate a broadband submillimeter wave signal centered at 1 THz through optical rectification. In acentric materials the dominant contribution to optical rectification is the inverse electro-optic effect, in which an incident optical field, interacting with a nonlinear material, generates an outgoing field of the same optical frequency, and a d.c. polarization. When short optical pulses with appreciable bandwidths are used in the experiments, a freely radiating millimeter-wave polarization is created in the material, which can be detected using a metal dipole antenna. **Figure 15** shows the temporal pulse detected by a dipole antenna in the far field, along with its Fourier transform. The amplitude of the detected signal is almost 200 times larger than the signal detected from Lithium Tantalate, indicating a very large nonlinear optical susceptibility in this microwave frequency range. Strong resonances in the detected submillimeter-wave spectrum may be attributed to vibrational enhancement of the nonlinear optical coefficient, multiple fresnel reflections of the submillimeter-wave beam in the crystal, or nonlinear frequency chirping of the submillimeter-wave field. The lack of any significant structure in signal spectra taken with inorganic materials such as Lithium Tantalate or GaAs indicates that vibrational contributions to the detected signal are likely in molecular crystals. If molecular crystals exhibit strong coupling between vibrational modes and the macroscopic electronic hyperpolarizability, applications requiring high-speed electro-optic modulation may benefit from these resonances. The spectral locations and strengths of strong signal enhancement may be tunable through crystal structure or chromophore modifications, which would enhance the modulation efficiency of narrow-band electro-optic modulators operating above 100 GHz.

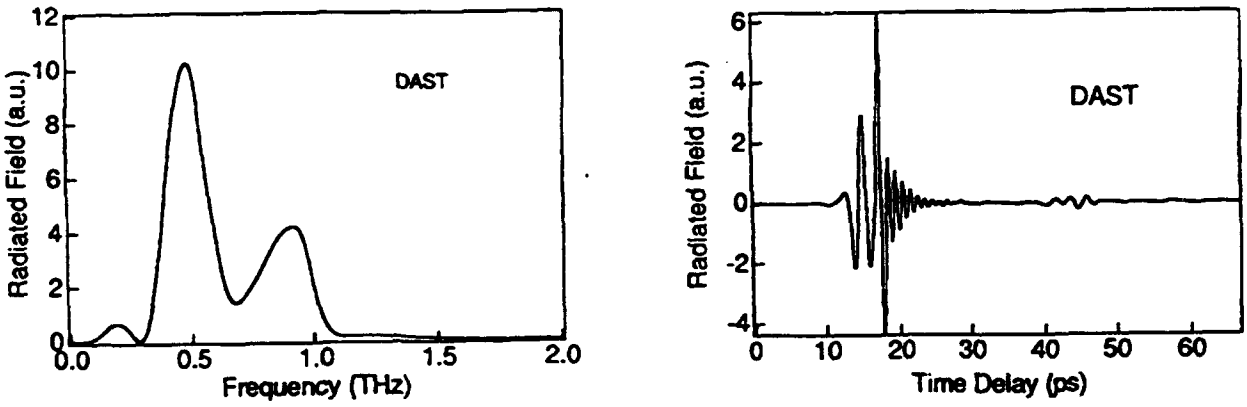

Figure 15: Fourier Transform of Temporal Radiation Waveform from Optical Rectification for DAST.

Optical Damage

Optical absorption caused by one or multi-photon transitions is deleterious to useful modulator operation when considering their use in high optical power applications. Experiments were performed to determine if thermal loading limits the optical power handling capability of highly colored organic salts such as DAST. A CW Ti:sapphire laser output beam was focused to a 2 μm diameter spot and the wavelength tuned from 700 - 1000 nm. The transmitted optical power was monitored as a function of wavelength and polarization, and the fresnel reflection losses were added to the transmitted power. Within experimental error, no differences were observed between the experimental optical transmission and the optical transmission calculated using Fresnel reflection losses in a transparent medium, indicating that over this wavelength range, the absorption coefficient was $<0.2\ cm^{-1}$.

With the same experimental setup, the optical threshold for catastrophic material damage was determined, the results of which are shown in **Figure 16**. Critical to the measurement of high optical damage thresholds was the careful cleaning of crystal surfaces prior to testing. For example, the presence of a hydrate film on the crystal surface resulted in catastrophic damage thresholds several times lower than the quoted values. With a CW Ti:sapphire laser, the CW damage threshold ranged from $<3\ MW/cm^2$ at 700 nm when polarized along the polar a-axis, to $>30\ MW/cm^2$ at 800 nm when polarized perpendicular to the polar axis. The latter measurement was made with 1 W cw optical power focused to a 2 μm diameter spot on the crystal surface. Note that above 750 nm, the maximum average power plotted in **Figure 16** is limited by the laser, rather than optical damage of the sample. The data above 750 nm therefore represent lower limits to the optical damage thresholds. When the laser ran in a femtosecond mode, the CW damage thresholds were similar, giving peak power damage thresholds of $>30\ GW/cm^2$ at 800 nm. With these optical peak powers, a variety of nonlinear effects were observed. Additional measurements were carried out at 1.06 microns using a cw-modelocked Nd:YAG laser (pulsewidth = 80 psec). At the maximum available power of 8.1 W, DAST did not damage when the beam was focused to a 0.5 mm diameter spot. Second harmonic generation at 532 nm was observed in reflection and in transmission. This corresponds to a peak power of $600\ kW/cm^2$.

The damage thresholds of DAST were excellent when compared with other commonly used nonlinear optical materials. **Table 2,** below, gives a comparison between DAST and several common nonlinear compounds. Several properties could be contributing to the surprisingly good damage thresholds seen in DAST. First, DAST has a high melting point (259 °C) compared with other organic materials, allowing it to handle a higher thermal gradient across the beam diameter than other organic compounds. Second, the ionic structure of DAST gives it better mechanical robustness than organic crystals held together through covalent interactions between chromophores. The ionic compound also tends to self-purify as it is grown from room temperature solutions, resulting in lower impurity absorption than inorganic compounds grown from high-temperature melts.

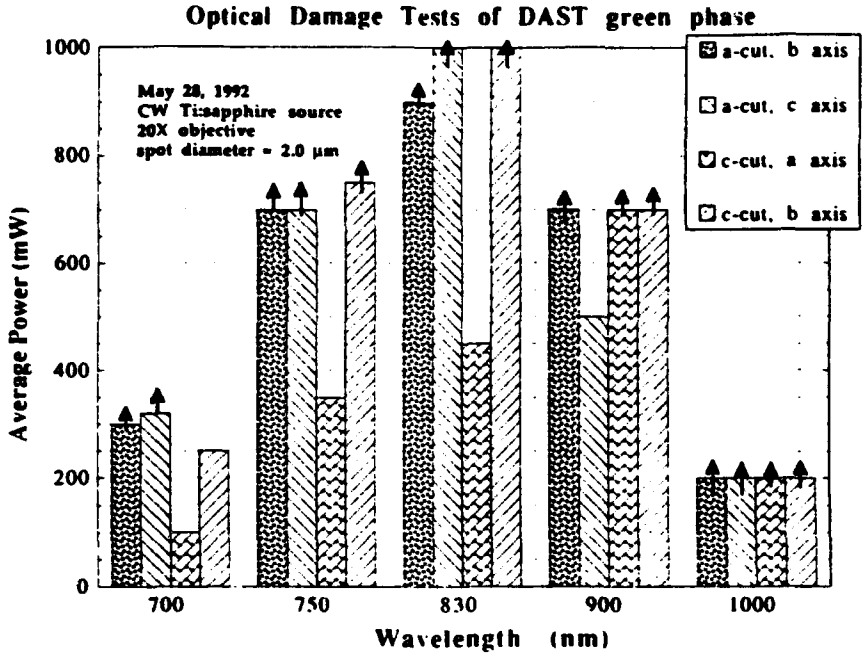

Figure 16: Optical Damage Tests of DAST.

Table 2: Comparisons of Optical Damage Threshold.

Material	Damage Threshold*
Lithium Niobate (inorganic)	CW- 5 - 10 MW/cm^2 @ 0.8 µm Q (30 nsec)- 4 J/cm^2 @ 1.06 µm ML (1 psec)- 70 GW/cm^2 @ 0.6 µm
DAST (organic)	CW - 10-30 MW/cm^2 @ 0.8 µm ML (0.1 psec)- 30 GW/cm^2 @ 0.8 µm
mNA (Meta-Nitroaniline) (organic)	CW - 10 W/cm^2 @ 1.06 µm Q (20 nsec)- 4 J/cm^2 @ 1.06 µm
POM (3-Methyl-4-Nitropyridine-1-Oxide) (organic)	Q (15 nsec)- 0.75 J/cm^2 @ 0.53 µm ML (20 psec)- 2 GW/cm^2 @ 1.06 µm

*CW- continuous-wave
Q- nsec repetitively pulsed
ML- psec or fsec pulse-train

Thermal Stability

Determination of the electrical and thermal stability of DAST and related salts is also critical to their use in actual devices. In particular, long-term thermal stability has been the bane of organic nonlinear materials. For ionic salts such as DAST, differential scanning calorimetry (DSC) and thermo-gravimetric analysis (TGA), as shown in **Figure 17**, have demonstrated the thermal stability of several organic salts. However, these tests are only short-term, and say nothing about the long-term thermal stability of single crystals. To investigate this, crystals of DAST were bonded with a commercial U.V. curing epoxy onto quartz substrates, and maintained in room air at 145 °C for 3300 hours. Changes in crystal properties due to thermal aging were determined through changes in the optical absorption spectra, observation of the crystal facets to detect any decomposition or solid-state diffusion at the epoxy-crystal interface, and optical birefringence anomalies. The epoxies used for this experiment changed over the course of the experiment from clear to deep red, indicating considerable thermal damage. However, apart from bulk cracks induced by differential thermal expansion between the crystals and the epoxy, the DAST crystals appeared unchanged after this exposure.

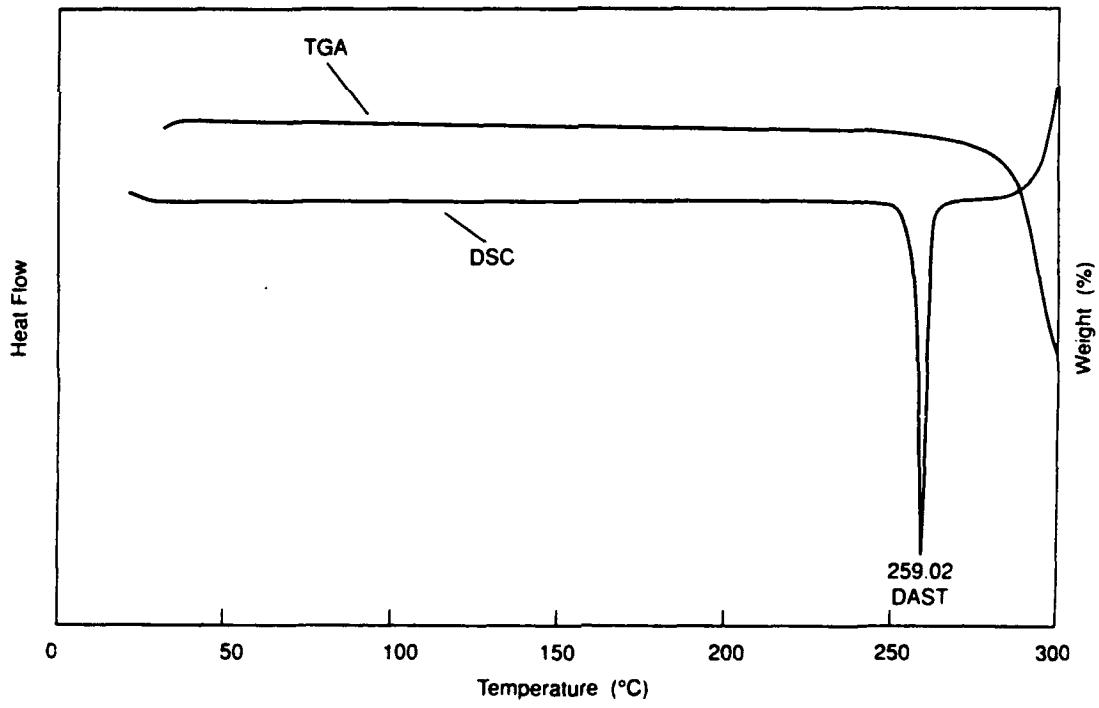

Figure 17: Differential Scanning Calorimetry and Thermal Gravimetric Analysis of DAST Crystals.

Electrical Properties

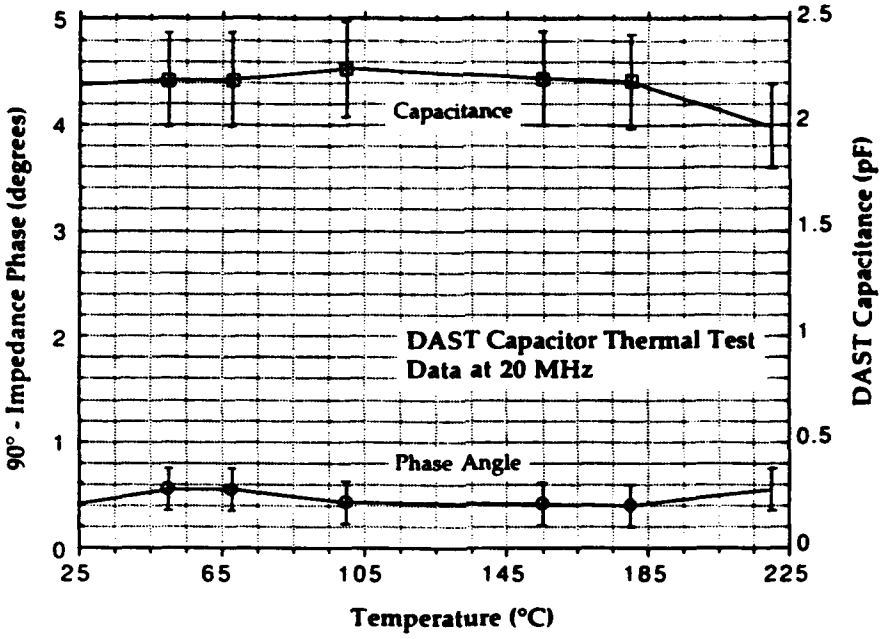

Figure 18: Electrical Properties of DAST at Elevated Temperatures.

The electrical properties of DAST have been monitored at elevated temperatures over short times (several hours). A sensitive measure of dielectric failure involves monitoring the complex dielectric constant of a sample, by measuring the capacitance and loss tangent of a parallel plate capacitor formed from the material being tested. A network analyzer (HP 3577A) with a frequency range of 1 MHz - 100 MHz was configured as an impedance analyzer and used to monitor changes in a small capacitor formed by sandwiching a DAST crystalline plate between two electrodes. The capacitor was mounted on a hot plate and heated slowly from room temperature to the melting point. The capacitor's impedance was measured over the entire frequency range at regular temperature intervals. A plot of a portion of the data is shown in **Figure 18** for measurements made at 10 MHz (data at other frequencies are identical). The loss tangent remains below 0.5 degrees, the resolution of the equipment used, and the capacitance remains essentially unchanged up to temperatures of 220 °C. Although finer loss tangent resolution is desirable to quantify the dielectric loss of DAST, it is clear from this experiment that the loss tangent is small, and remains small up to temperatures in excess of 200 °C.

High Frequency Dielectric Response of DAST:

The dielectric properties of DAST were measured in the microwave and mm wave regions. The microwave measurements were made using a conventional phase delay measurement and a two-port network analyzer. The

measurements in the THz region were performed using a femtosecond optical pump/probe experiment arrangement. From these experiments, the best available dielectric constants for DAST in the microwave regime are $\epsilon_a = 8.0$, $\epsilon_b = 2.9$ and $\epsilon_c = 2.9$. In the sub-mm wave regime, these values are altered to $\epsilon_a = 7.0$, $\epsilon_b = 4.0$ and $\epsilon_c = 4.0$. These values are consistent with the low frequency dielectric constants measured previously, and indicate that the dielectric dispersion from D.C. to 1 THz is small, an advantage when designing broad-band electrooptic modulators.

The microwave experiments were carried out using a rectangular waveguide adapter connected to an HP8510B network analyzer. Phase shift measurements vs. frequency were made from 2-20 GHz. The sample thickness was adjusted so that $L < \lambda / (4 \epsilon_a)^{0.5}$ over the wavelength range of interest (2.5 mm for DAST). Several samples of polycrystalline DAST were blended to a 25% or 50% wt/wt with an epoxy host and the cured monoliths were machined to the desired dimensions. The 25% wt/wt sample gave the most consistent results, with $\epsilon_{sample} = 3.35$, compared with an epoxy dielectric constant of $\epsilon_{epoxy} = 3.09$. This results in an orientationally averaged for 100% DAST of $\epsilon_{avg} = 4.1$. No unusual resonances were observed over the frequency range of 2-20 GHz.

A second measurement consisted of placing single crystals of DAST in a Styrofoam mold which then fit into the waveguide. The DAST crystals were oriented to allow probing of the principal dielectric constant ϵ_c ($= \epsilon_b$). Typical values measured were $\epsilon_c = 2.9 - j\ 0.004$ and $\mu_c = 1.09 + j\ 0.014$. Since the wave guide mode was TM_{00}, the electric field was polarized along the waveguide axis.

The remaining two principal dielectric constants were then calculated using the relation

$$\epsilon_{avg} = \{ \epsilon_c / 2\ p \}\ \ln[(1 + p) / (1-p)$$

where

$$p = [\ 1 - \epsilon_c / \epsilon_a\ ]^{0.5}$$

Using the measurements above, the dielectric constants are $\epsilon_a = 8.0$, $\epsilon_b = 2.9$ and $\epsilon_c = 2.9$. These values are consistent with the low frequency dielectric measurements reported in our previous annual report.

THz frequency measurements of the dielectric constant were performed at RPI in Troy, NY. The experiment consists of focusing a fsec pulsed infrared Ti:sapphire laser onto a sample of DAST, which is transparent in the near-

infrared. Co-propagating optical and THz pulses emerge from the crystal, which then pass through a D.C. biased GaAs wafer. The infrared pulse passes through the GaAs, generating a THz pulse. The THz pulse generated in the DAST sample passes through the GaAs sample. A photoconductive optically triggered antenna detects the arrival of both THz pulses. The arrival times of the two pulses will not coincide if the THz and optical pulses see different group refractive indices in the DAST sample (it is assumed that the THz signal is generated near the entrance surface of the DAST, and that DAST is sufficiently thick that its entire thickness can be used with the time delay to calculate group velocities for the THz pulse). When performed on a 1.72 mm thick sample of DAST, the data shown in **Figure 19** was collected, indicating that the group dielectric constants and refractive indices are:

$N_a = 3.36$ $\quad$ $N_b = 1.82$

$\epsilon_a = 6.4$ $\quad$ $\epsilon_b = 4.3$

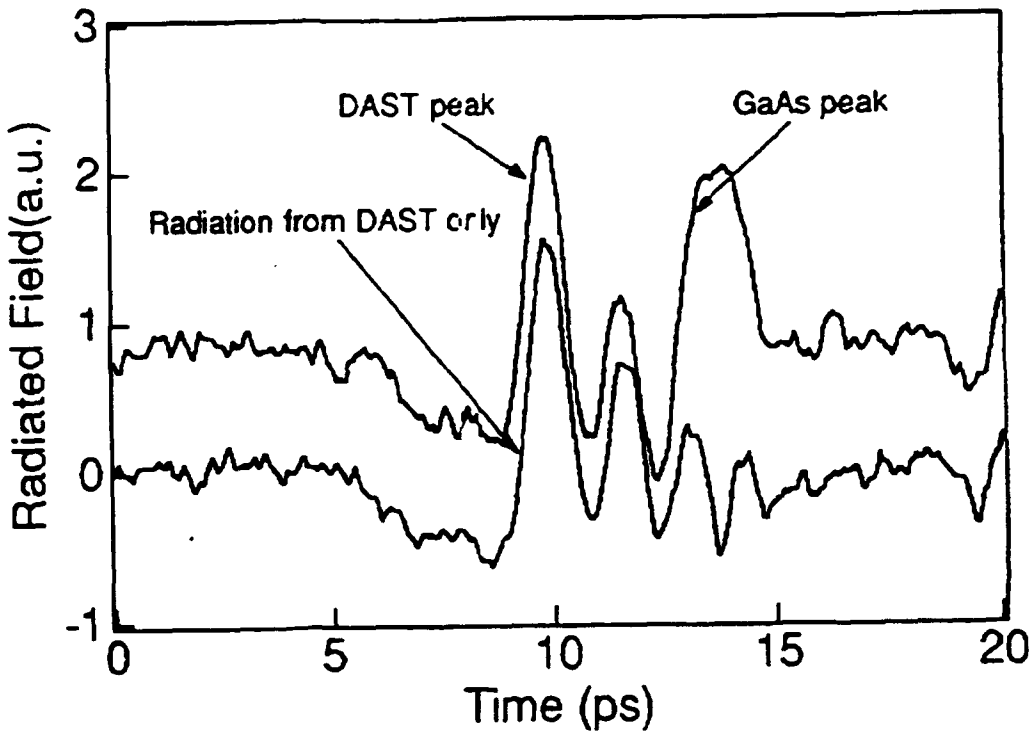

Figure 19: THz Frequency Measurements of Dielectric Constants.

To corroborate the optical results, white-light interferograms were measured at 670 nm, 820 nm and 930 nm, and compared with the group refractive indices predicted from the refractive index Sellmeier equations for DAST via

$$N_{a,b,c} = n_{a,b,c}(\lambda) - \lambda \, dn_{a,b,c}(\lambda)/d\lambda$$

Figure 20 shows one example of a white-light interferogram measured on a DAST single crystal at 670 nm, indicating a group refractive index of N_a = 5.09. **Figure 21** shows the Sellmeier curves for n_a and n_b, the calculated group refractive indices N_a and N_b , and the experimental data points. The overall agreement is very good except near 800 nm. We attribute this to a subsidiary absorption peak centered near 650 nm, which will increase the group refractive index slightly in the 700 - 900 nm range. This subsidiary absorption peak was not included in the Sellmeier fit to the refractive index data.

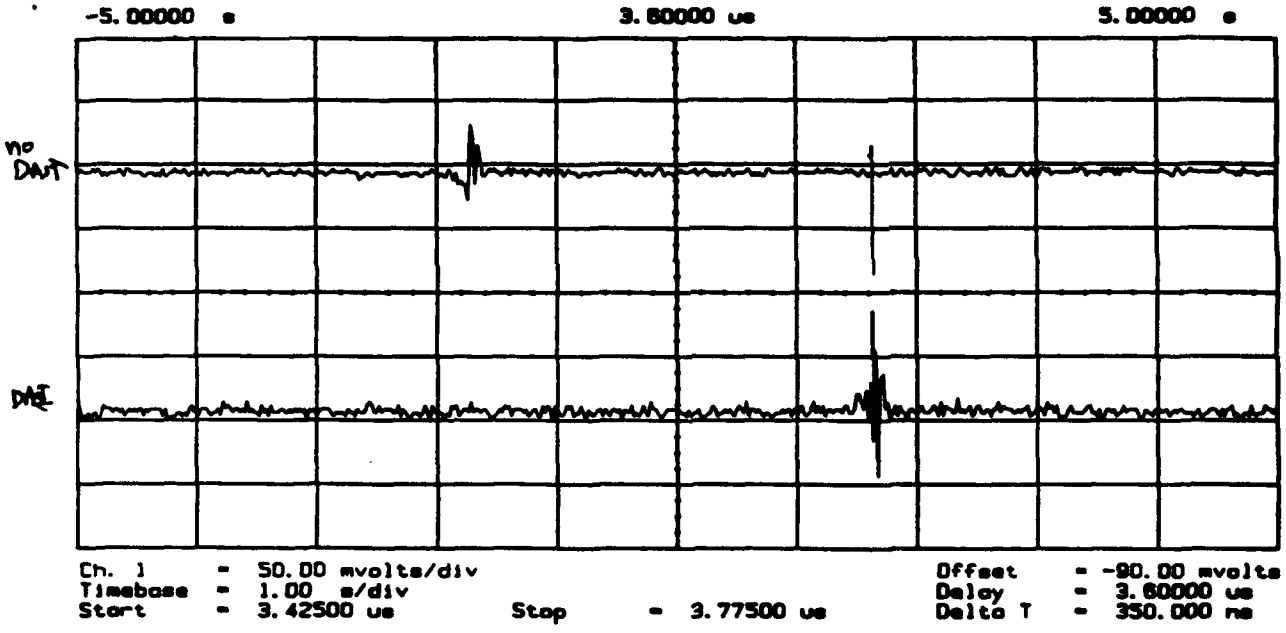

Figure 20: White Light Interferogram of DAST at 670 nm.

The group refractive index has important implications for high speed modulators. If a train of optical pulses entering an electro-optic modulator is to be modulated efficiently, then the velocity of the applied modulating EM field must travel synchronously with the optical pulse, i.e. the group velocities of these two signals must be matched. In conventional materials such as Lithium Niobate, this cannot be achieved because of the relatively low optical group refractive index (2.3-2.4) compared with the higher group refractive index at mm wave frequencies (5-5.5). In DAST, however, the mm-wave signal has a lower refractive index than the optical pulse throughout most of the near infrared region. By choosing the waveguide dispersion and/or selecting an appropriate operating wavelength, the two group refractive indices can be matched, allowing much more efficient modulation of the optical signal. For example, with light polarized parallel to the a-axis in DAST, the group refractive indices are matched (and equal to 2.6) in the 800 - 1000 nm wavelength range. This is a significant advantage for high speed electro-optic modulators based on DAST.

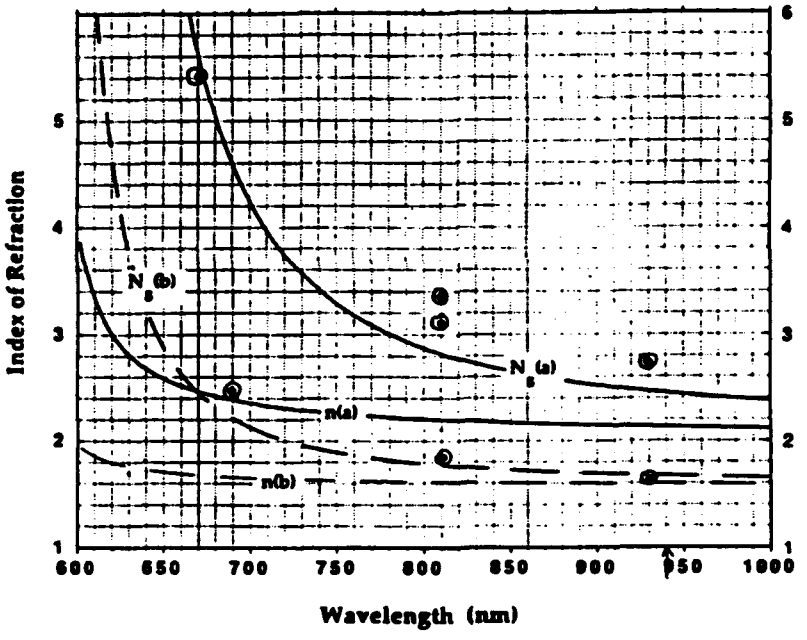

Figure 21: Refractive Indices for DAST

These results were reported at the Optical Society of America Annual meeting to be held in Toronto, Canada from Oct. 4-6, 1993.

Nonlinear Optic Measurements of DAST:

As previously described, a tunable optical parametric oscillator was assembled based on a KTP crystal cut for operation from 1.2-2.0 μm using a 532 nm Nd:YAG pump laser. A typical Maker fringe setup was assembled to measure the d coefficients of materials relative to Lithium Niobate. A typical output spectrum for our OPO is shown in **Figure 22**. An instrument-limited linewidth of 4 cm^{-1} has been measured. This is an important issue when comparing the results measured with the OPO against measurements made using a Raman shifted optical source, since the latter has a much narrower linewidth.

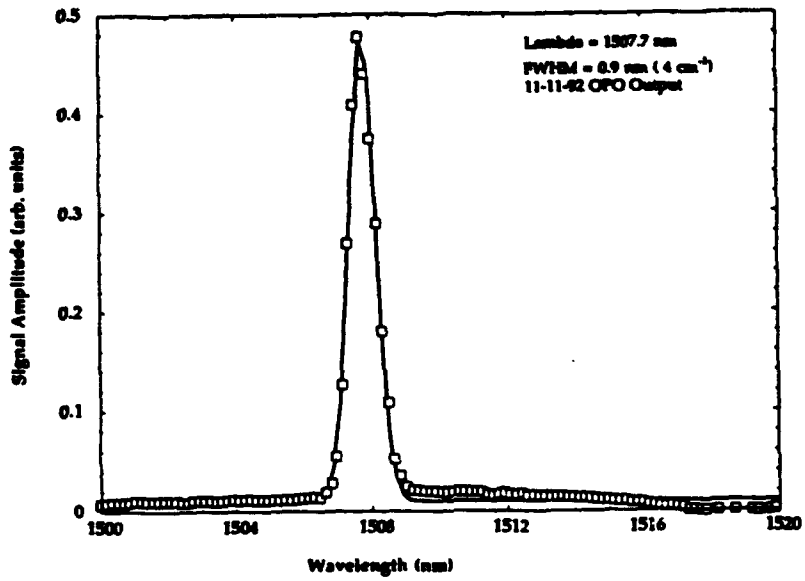

Figure 22: Typical Spectrum Showing OPO Output Linewidth.

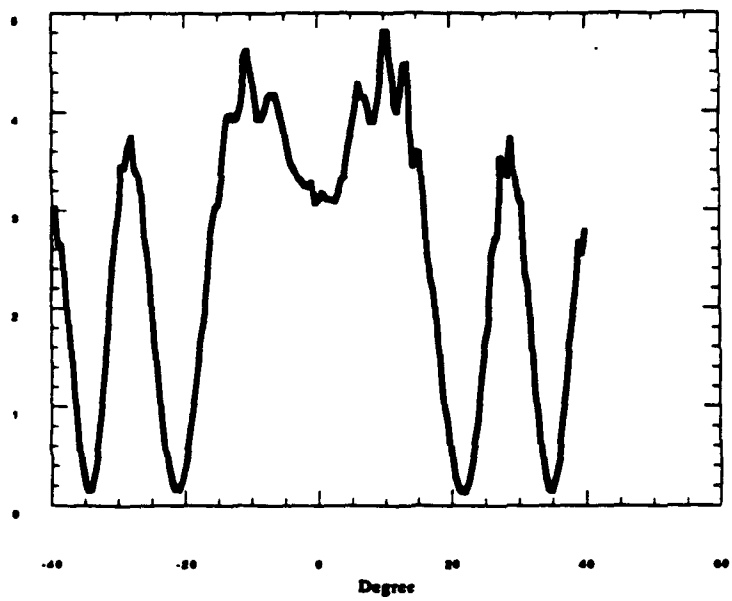

Figure 23: Maker Fringe Data for DAST at 1.6 μm.

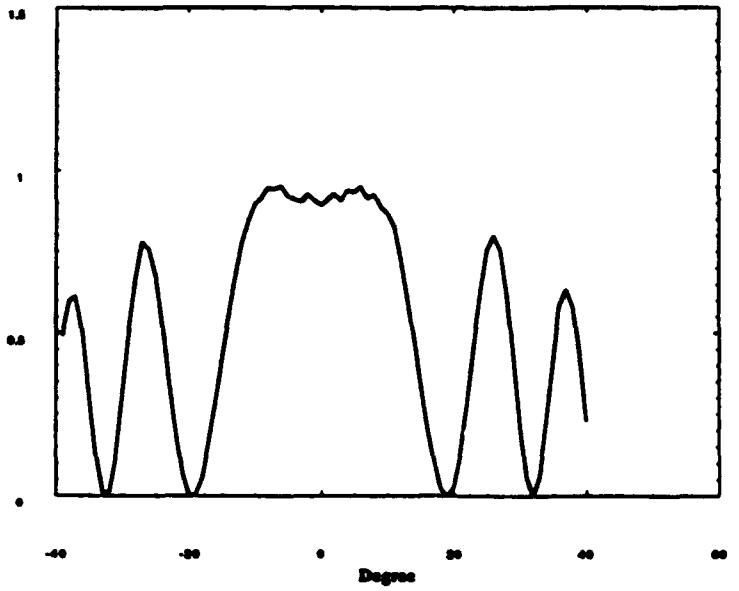

Figure 24: Maker Fringe Data for Lithium Niobate at 1.6 μm.

Figures 23 and **24** show typical Maker fringe results for DAST and Lithium Niobate, respectively at a wavelength of 1.6 μm. Data was collected from 1.2 to 1.9 μm and plotted in **Figure 25**. The data were fit with a conventional two-level gas-phase model used to predict the resonant enhancement of the nonlinearity in DAST. *The agreement is excellent.* The absolute magnitude of the nonlinearities measured were considerably lower than the values measured using the Raman-shifted output form a Nd:YAG laser. Typically, the variation from sample to sample was as much as a factor of two in nonlinear d coefficient, depending on the surface quality, crystal bulk quality and growth conditions. It is not clear at present what is affecting the nonlinearity from crystal to crystal. However, in a dispersive material, a very narrow bandwidth light source is needed to avoid phase matching wash-out within the crystal.

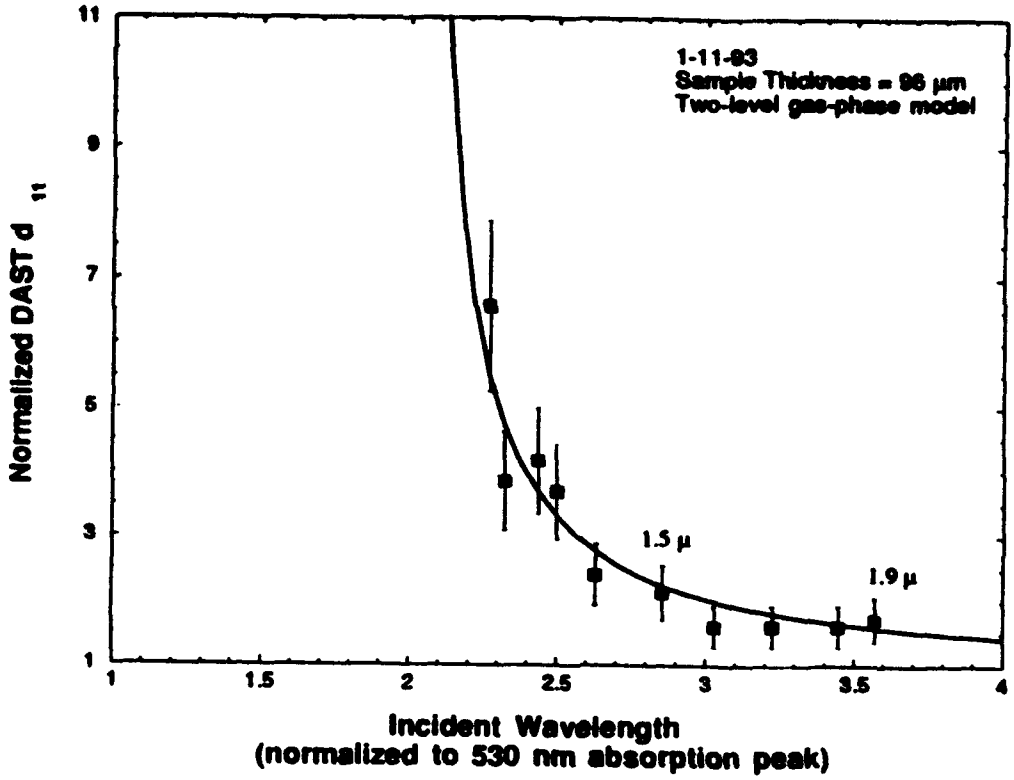

Figure 25: Resonance Enhancement of DAST d_{11}
Measured via Tunable Maker Fringe

While running Maker fringe at 1.2 μm, we discovered a phase-matching condition exists for the d_{26} coefficient of DAST (which at these wavelengths may only be ~10 pm/V). The incident optical field is polarized at 45° to the a-axis, and phase matching at normal incidence occurs where l=1.181 mm. This provides valuable data to corroborate the refractive indices along the a and b axes at 1.8 and 0.59 μm. Note that at 0.59 μm second harmonic wavelength. the b-axis is already absorbing quite strongly, and the a-axis is highly absorbing. **Figure 27** shown the phase matching curve achieved at l=1.181 μm, and **Figure 26** is a photograph of the second harmonic signal exiting the crystal. The central spot is surrounded by the three phase-matching loci, one circular and the other two ellipsoidal. At l =1.18 μm, the intersection points of the one ellipse and circle coincide with the central spot. The phase matching loci are typical for a strongly biaxial crystal, or for a twinned crystal. It is highly likely that this particular crystal was composed of two crystal plates with the a axes oriented in an antiparallel configuration.

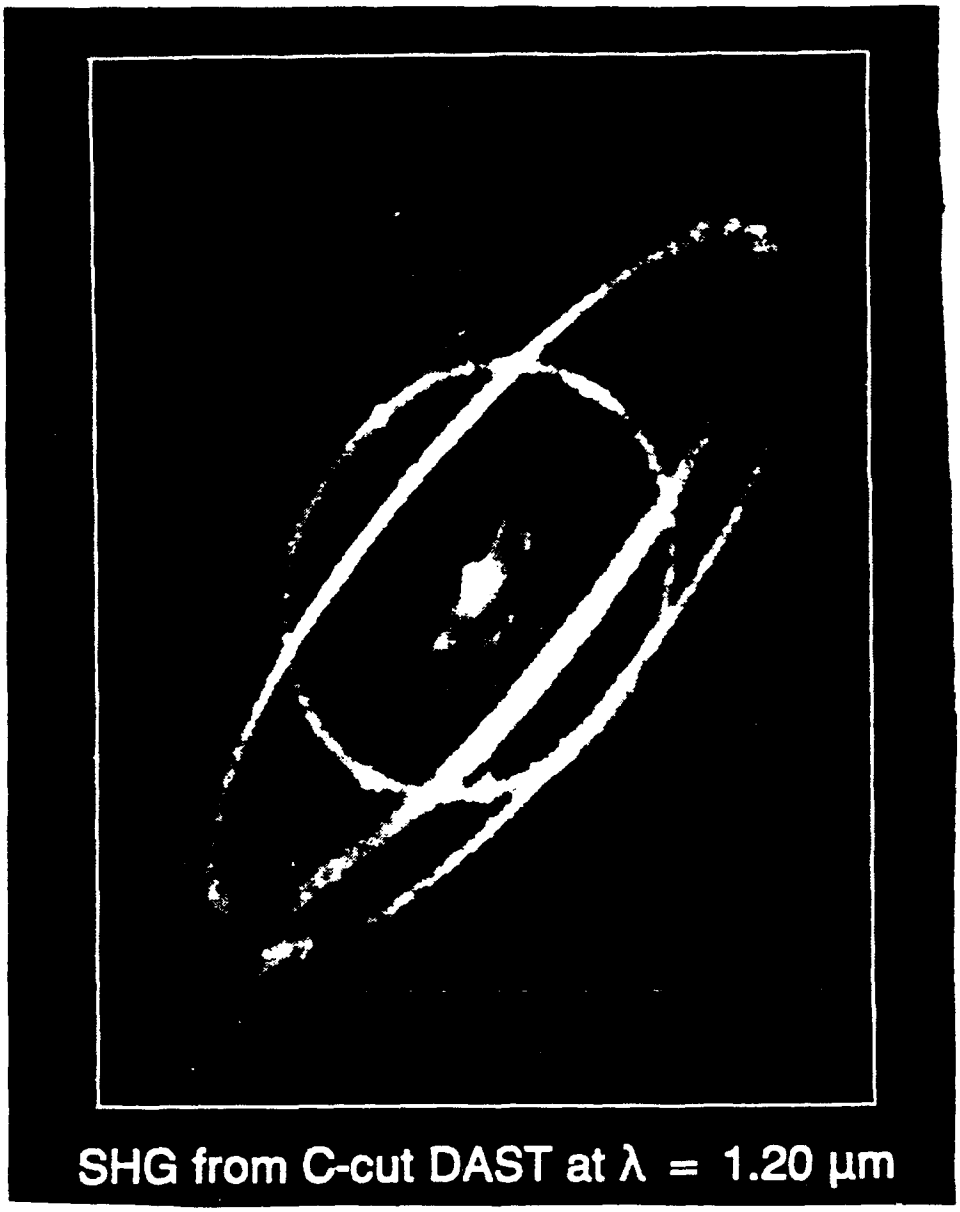

Figure 26: Photograph of Second Harmonic Signal From DAST
At l = 1.181 μm Showing Phase Matching Loci.

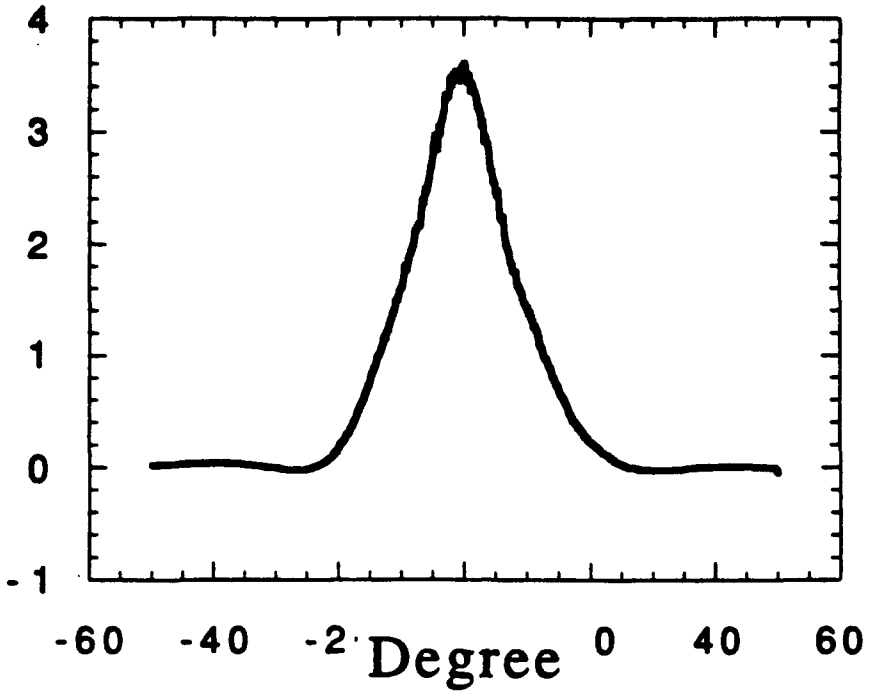

Figure 27: DAST Phase Matching At l = 1.181 μm.

Figure 28 shows the Sellmeier equations for the refractive indices of DAST, and the wavelength range over which phase matching was observed. The agreement between the observed phase matching behavior and the refractive indices previously measured is good.

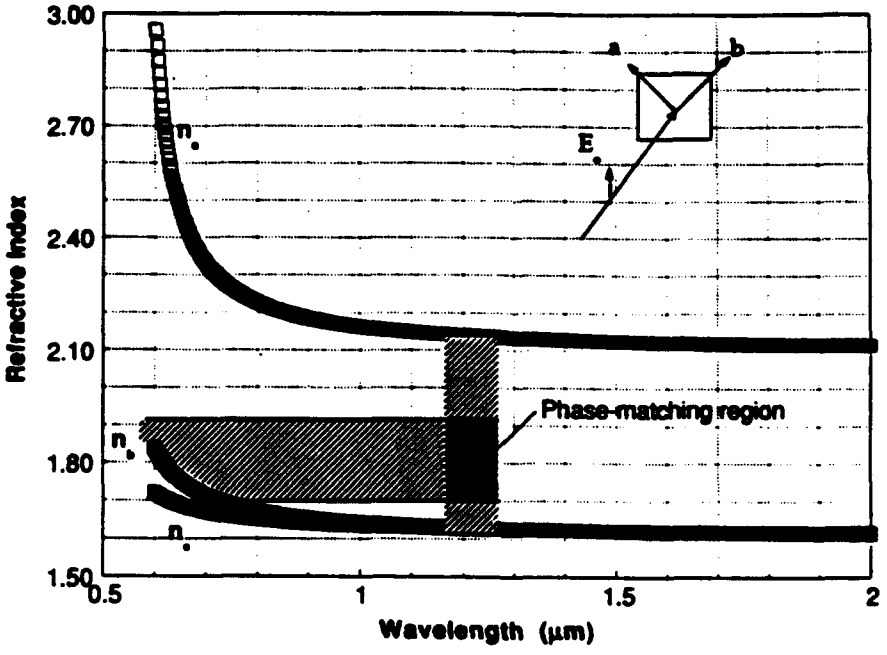

Figure 28: Dast Refractive Indices

Dispersion of Nonlinear Susceptibility in DAST:

With a value of d_{33} (lithium niobate) = 30 pm/V, the dispersion of d_{11} in DAST was measured from 1.2 μm to 1.9 μm. The data were previously shown in **Figure 25** on page 32 of this report. Each data point was extracted from the Maker Fringe best fit of the equation listed above, using Sellmeier data for the refractive indices of DAST and a sample thickness of L = 96 μm. An example of the fringes generated by the experiment are shown at a wavelength of 1.5 μm in **Figure 29**. This sample gave typical SHG signals- that is, there were samples which signals as much as a factor of 4 larger and as much as a factor of 3 smaller.

The data in **Figure 25** also included correction factors for the optical absorption of the second harmonic light. This was particularly important for incident wavelengths near 1.2-1.3 μm, where the second harmonic near 0.6-0.65 μm is well into the absorption edge of DAST for light polarized along the polar a axis. Because the refractive indices are also large, the resulting Fresnel coefficients are large and must be included to accurately fit the data.

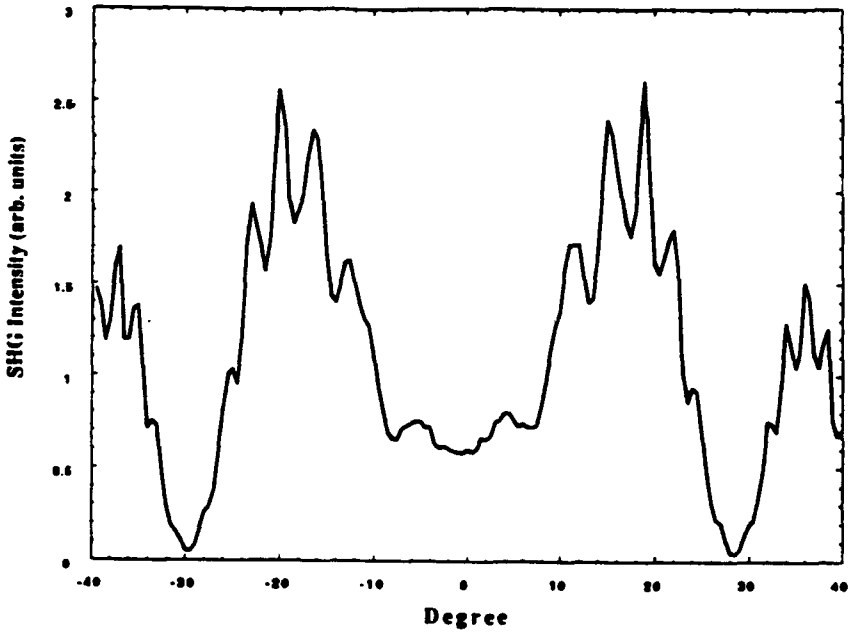

Figure 29: Maker Fringe Data for DAST at l = 1.5 μm.

Nevertheless, when a two-level gas-phase model for second harmonic generation resonance enhancement is superimposed on the collected data, having the form

$$F = E^4/\{(E^2 - (h\nu)^2)\ (E^2 - (2h\nu)^2)\}$$

where F is the resonance enhancement factor, E is the dominant transition energy, and (hν) is the incident photon energy, excellent agreement with the data is observed. This indicates that in DAST over this wavelength range, the chromophores are acting as individual nonlinear entities held in an aligned format with only minimal interaction between orbitals in physically adjacent chromophores.

Note that the y-axis in **Figure 25** is the normalized d_{11} coefficient. For this particular crystal, the absolute coefficient at zero frequency (resonance enhancement F = 1) relative to lithium niobate is d_{11} = 220 pm/V +/- 50 pm/V. This value is about a factor of 1.4 smaller than the zero-frequency coefficient of d_{11} = 310 pm/V +/- 100 pm/V (corresponding to d_{11} = 500 pm/V +/- 200 pm/V at 1.9 μm) previously reported for DAST using a Raman cell measurement at 1.907 μm. Since these measurements were made on different samples, we decided to investigate the variations in sample response for a variety of crystals grown by various means. The table below shows the variations in second harmonic signal and d_{11} for a variety of samples.

DAST Sample	Growth conditions	SHG Amplitude (arb units)	d_{11} (pm/V) @ 1.6 μm	
#2 L = 198 μm	30 °C bath	13.5	600	
#2 L = 198 μm	30 °C bath	11.9	560	
#3 L = 512 μm	50 °C	3 (FC = 0.15)	280	(400)
#4 L = 265 μm	B2-4 (20°C),dry	5.5	390	
#5 L = 183 μm	B2-4 (20°C),dry	15 (FC = 0.25)	630	(820)
#7 L = 221 μm	Room temp.	3.5 (FC = 0.3)	305	(400)
#8 L = 325 μm	Room temp.	2.4 (FC = 0.4)	250	(320)
#10 L = 110 μm	50 °C, old set	4.5	350	

The values in brackets are corrected values of d_{11} based on extrapolating the real fringe height from the reduced fringe contrast (FC) listed in the SHG amplitude column. Even with this correction included, the d_{11} coefficient at 1.6 μm varies from 320 pm/V to 820 pm/V, a factor of almost 3. Generally, thicker crystals tend to have washed out fringes and reduced NLO coefficients, reflecting the poor optical quality of the input and output facets, and internal stress induced birefringence in the crystals. The thinner crystals also tend to have sweet spots near the edges of the crystal. This is likely caused by crystal twinning in these samples. Near the edge of the samples, the twins are not always overlapped, allowing one of the twinned crystals to be accessed by the optical probe. When this occurs, large, clean fringes are observed, such as those shown in **Figure 29**.

Unfortunately, the twinned crystals tend to have the cleanest facets, allowing very clean probe beam propagation through the crystal. Correlations with crystal growth conditions are difficult to make at this point, although a slight trend indicates that crystal growth at lower temperatures is preferable to maximize the NLO coefficients (through improvements in the physical quality of the grown crystal).

Optical Modulators Using DAST:

During device fabrication, exposure of the crystalline material to a variety of solvents, temperatures, adhesives and metals will need to occur. The sensitivity of organic crystals to many of these compounds has traditionally excluded them from being used in devices. The difficulties in handling DAST and other organic salts were first identified, so that a compatible processing technique could be devised. In addition, the processing technique was chosen to allow fabrication of the device geometry desired. Since this is a multi-step process, the choices described below are a first approximation to the optimal processing techniques and modulator design choices.

Many organic salts are soluble to a greater or lesser degree in water, most solvents including alcohols, DMSO, acids, and some polymers. In addition, they tend to absorb some liquids (such as acetone or dioxane) readily into the surface, causing surface crazing or, in some instances, bulk cracks in the crystal. Based on these observations, a completely dry processing route was decided upon. Crystals which are grown in solution could be bonded directly to a substrate with an ultraviolet-curing epoxy. The crystal then needs to be machined to the appropriate geometry using a noncontact ablation process. After a plasma ash to clean up the crystal surface, electrodes would be evaporated onto the crystal surface through a shadow mask. With this approach, no solution processing is required. The geometric resolution possible is limited by the shadow masks used, typically 5 - 10 μm.

Compatibility of DAST with certain epoxides and solders has been demonstrated. DAST crystals have been soldered to metal surfaces using low temperature indium solders. This technique has been used to mount DAST in hermetically sealed laser diode packages and life-tested at 70 °C for 500 and 1000 hours. No changes in laser diode operation were observed. This crucial experiment is the first (to our knowledge) attempt to verify the compatibility of organic nonlinear materials and operating optoelectronic devices such as laser diodes over time.

Pockels Cell Modulator

The Pockels cell modulator structure was chosen as the first target because of its simplicity. As illustrated in **Figure 30**, the single pixel modulators consist of silver/chromium or gold/chromium electrodes evaporated directly onto a DAST single crystal oriented such that the incident optical field and the

applied low-frequency electric field are parallel to the polar *a* axis of the crystal. The electrodes were separated by 0.5-1.0 mm, and crystals with thickness of 0.3-1.0 mm were used. No surface passivation or protective coatings were used, and all tests were done in room air.

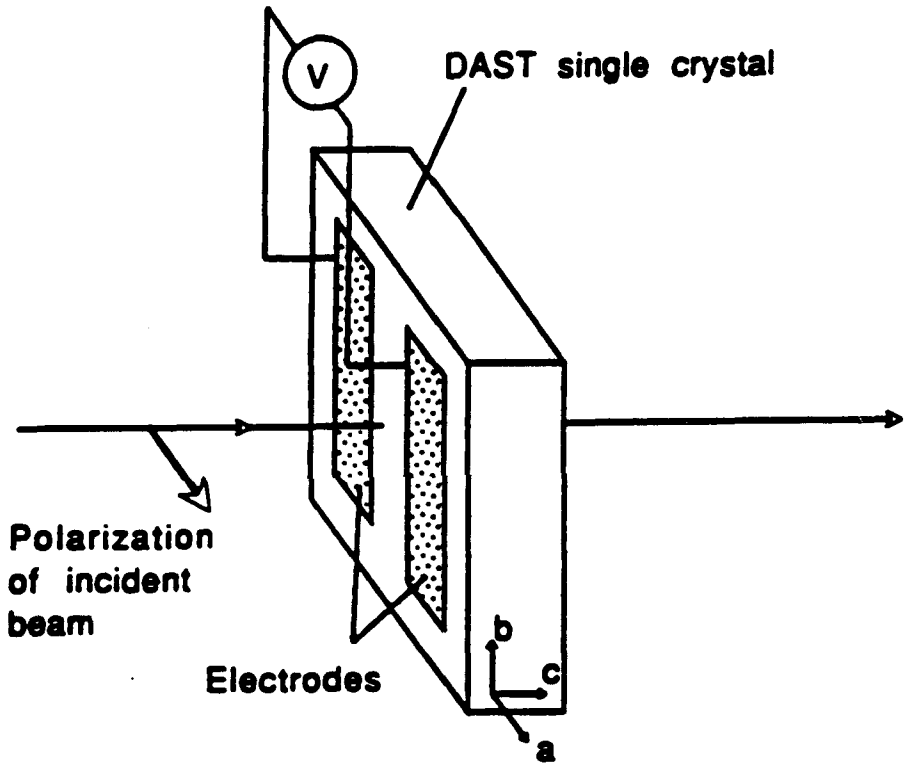

Figure 30: Schematic diagram of Pockels Cell Optical Modulator

The performance of these modulators was first tested at room temperature before being taken to higher temperatures. The electrodes were connected to a pulsed high voltage power supply. The crystal was mounted in one arm of a Mach-Zender interferometer, the incident light linearly polarized along the crystal polar axis. 50% unpolarized beamsplitters were used to split and

recombine the He-Ne beam. The recombined spot was expanded using a 10 cm focal length concave-concave lens, apertures and passed into a PIN silicon photodiode. The entire interferometer was mounted in a plastic covering box to minimize the effects of air currents on modulator operating point. Both unipolar and bipolar pulses were applied to the modulator.

Figure 31 shows the response of the modulator with a bipolar pulse of ±100 V. The contrast ratio shown in this figure is ~120:1.

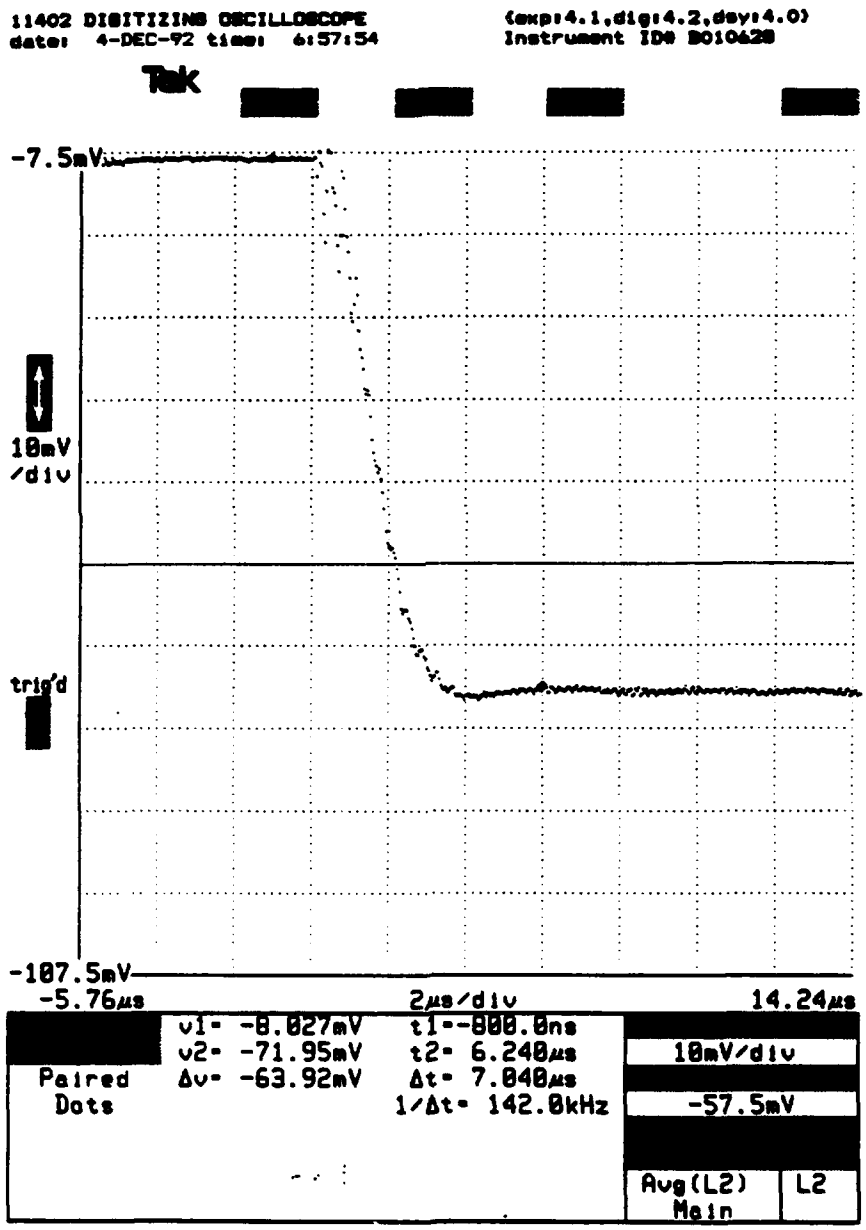

Figure 31: Simple Pockels Cell Response to 100V Bipolar Pulse.

As shown in **Figure 32,** under a constant applied field, the transmitted intensity initially reached a maximum value, but then very slowly decreased over time. When the field was reversed, the behavior was inverted. This indicates significant field screening caused by mobile charges in the crystal. It is very likely that solvent molecules are trapped between chromophore sheets during crystal growth. These may be removed by annealing the crystal.

The high speed response of these modulators was tested by substituting a high-speed HP pulse generator which provides 100 V peak voltage with a 20 nsec risetime. The signal was detected using a high speed Si PIN diode. (Thorlabs). The response is shown is **Figure 33.** The response is limited by the pulse source and photodiode bandwidth to ~ 20 nsec.

As a verification of the nonlinear coefficient of DAST, the applied voltage needed to achieve a π phase shift was 200 V. With an electrode gap of 0.56 mm and a thickness of 0.29 mm at 633 nm, the resulting Pockels coefficient is r_{11} = 292 pm/V. This is significantly lower than previously reported value of 400 pm/V measured at 820 nm. The more recent value is also not consistent with measurements made at Stanford University (r_{11} ~ 80 pm/V @ 633 nm), the Jet Propulsion Laboratory (r_{11} ~ 50 pm/V @ 1064 nm), and ETH (r_{11} ~ 100 pm/V @ 800 nm). However, based on resonant enhancement of the nonlinearity and the nonlinear susceptibility measured via Maker fringe technique at 1.907 μm, these values are consistent with r_{11} ~ 500 pm/V @ 633 nm and r_{11} ~ 210 pm / V @820nm. The reasons for the large discrepancies continue to be explored. It is possible that piezoelectric contributions to the original results may have resulted in measured responses which were incorrectly interpreted as being solely due to the Pockels effect. There are also inconsistencies between the values measured for DAST at 633 nm and the values measured for the related salt, Dimethylamino Stilbazolium Methylsulfate originally reported by Toshimura in 1988.

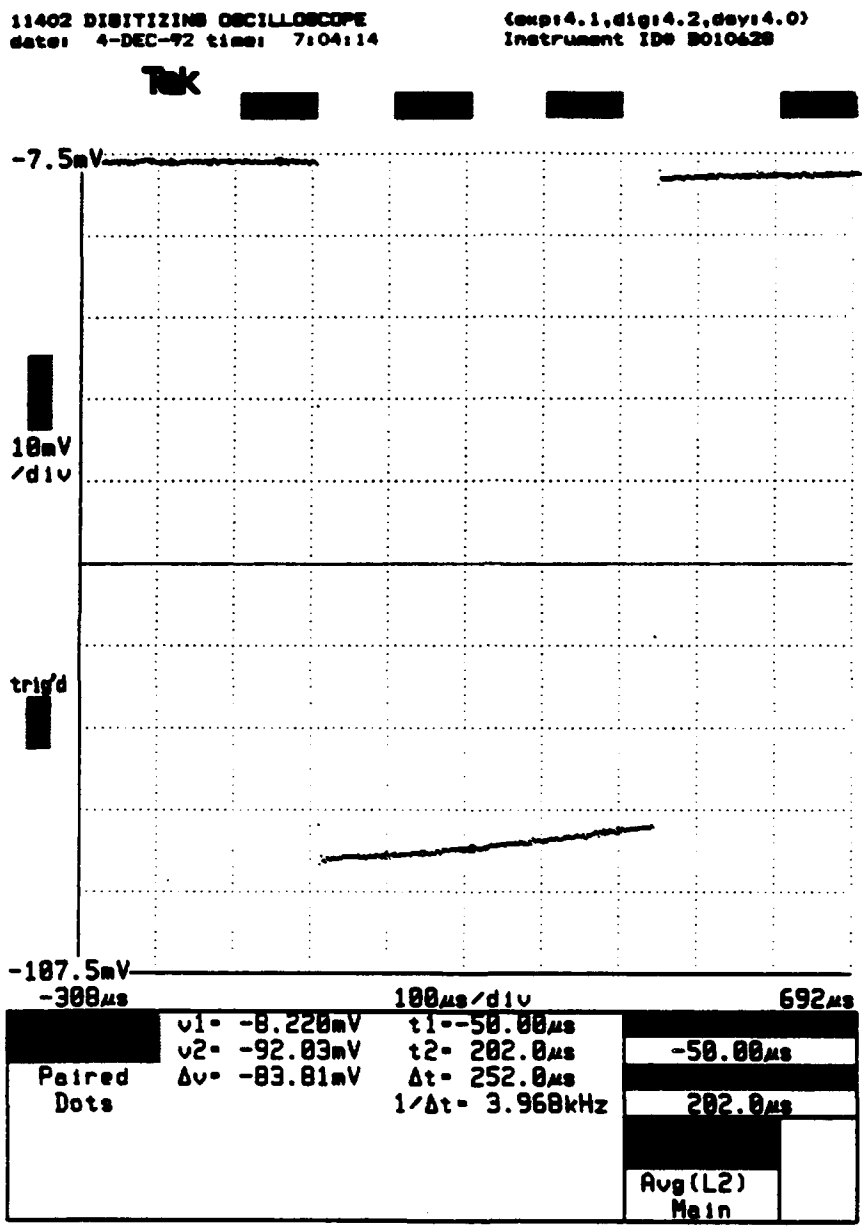

Figure 32: Pockels Cell Response to Constant Applied Voltage.

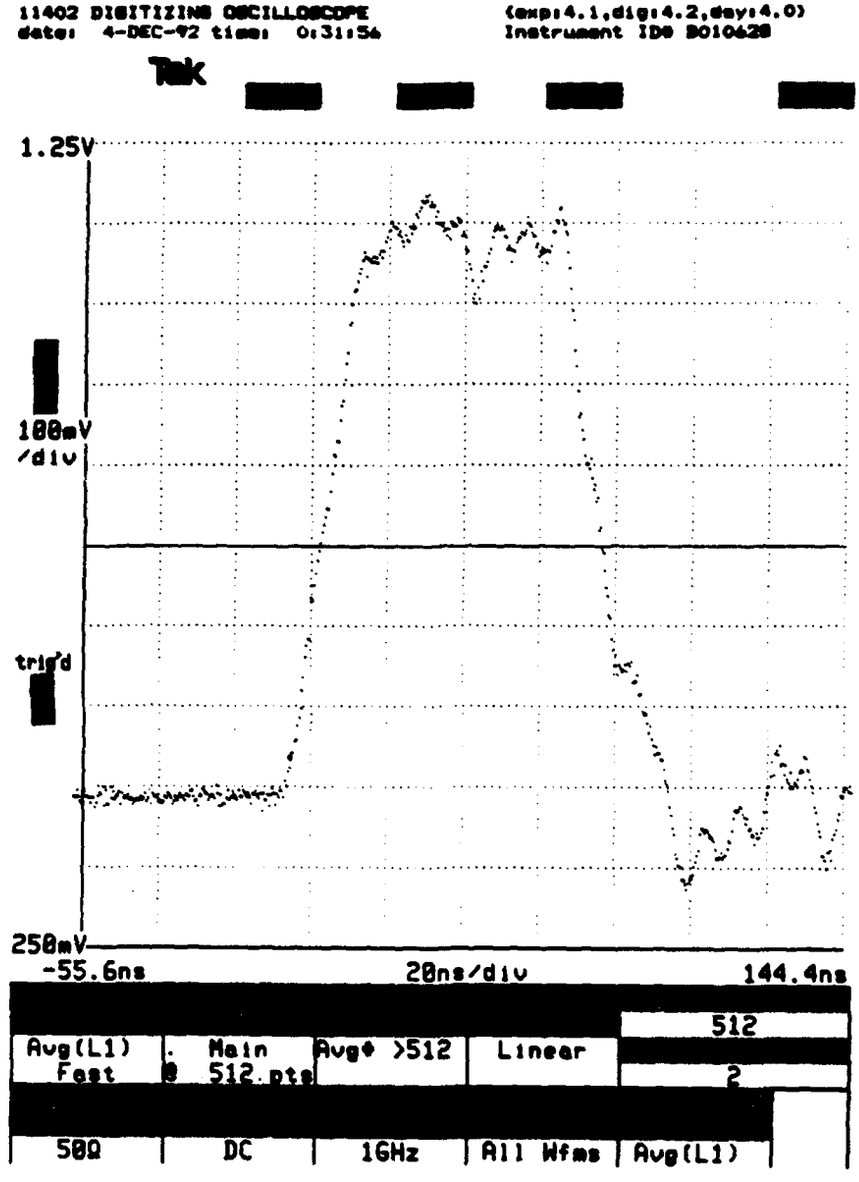

Figure 33: High Speed Response of DAST Pockels Cell.

Linear Array of Fabry Perot Etalon Modulators

A design has been chosen for the linear array modulators. As shown in **Figure 34**, the modulators consist of a Fabry-Perot cavity containing DAST, with electrodes contacting the sides of the crystal. Dielectric mirrors can be contacted to the crystal to form the complete device. Incoming light polarized parallel to the crystalline *a* axis is phase-shifted by the applied electric field, resulting in a change in the optical cavity length, and if properly biased on the side of a transmittance peak, a change in the transmitted and reflected optical intensities. With this design, we anticipate drive voltages significantly below 100 volts to achieve a 100:1 contrast ratio. Based on this design, the processing steps outlined below were developed and tested. Initial modulator structures having pixel sizes of 200 - 300 μm, cavity lengths of 300 - 500 μm, and electrodes suitable for driving 8 pixels in a linear array have been fabricated.

The structure is shown in **Figure 34**, and consists of a single crystal of DAST sandwiched between two dielectric mirrors and having two electrodes coating opposite sides of the crystal. The applied electric field is transverse to the direction of optical propagation. Incident light is polarized parallel to the *a*-axis of the DAST crystal, which also lies in the plane of the structure. The electric field is also applied parallel to the *a*-axis to make use of the dominant r_{11} coefficient in DAST.

Initial modeling of the anticipated performance is shown in figures 35-38. In **Figure 35**, the transmittance of the modulator is plotted as a function of the applied voltage across the electrode pair. The target of 20 dB contrast ratio is indicated by the horizontal heavy line. The curves are plotted as a function of the distance between the two dielectric mirrors, which is filled with DAST. In this figure the reflectance of the mirrors was chosen to be R=0.9, the wavelength is 0.8 microns, the electrode spacing is 100 microns, the Pockels coefficient is r_{11} = 100 pm/V, and n_a = 2.2. The figure demonstrates that contrast ratios of 100:1 can be achieved at drive voltages well below 100 volts by using crystals with an aspect ratio (that is, the ratio of crystal length to crystal width) of more than 2:1, provided that the modulator is biased at peak transmission with no applied voltage.

Figure 36 shows the variation in transmittance as a function of applied voltage for a set of mirror reflectances at a fixed aspect ratio of 5:1. Again, we see that a mirror reflectance of at least R=0.9 is required to achieve 20 dB or better contrast ratios. **Figure 37** indicates the wavelength dependence of the modulator. In this case, the transmittance is plotted as a function of the applied optical wavelength for a series of modulator lengths. As the modulator length increases, the free spectral range of the cavity decreases, increasing its sensitivity to incident wavelength and reducing the wavelength acceptance window width. In this case, a short cavity length is advantageous for broad spectral acceptance, and therefore represents an important compromise in this modulator structure.

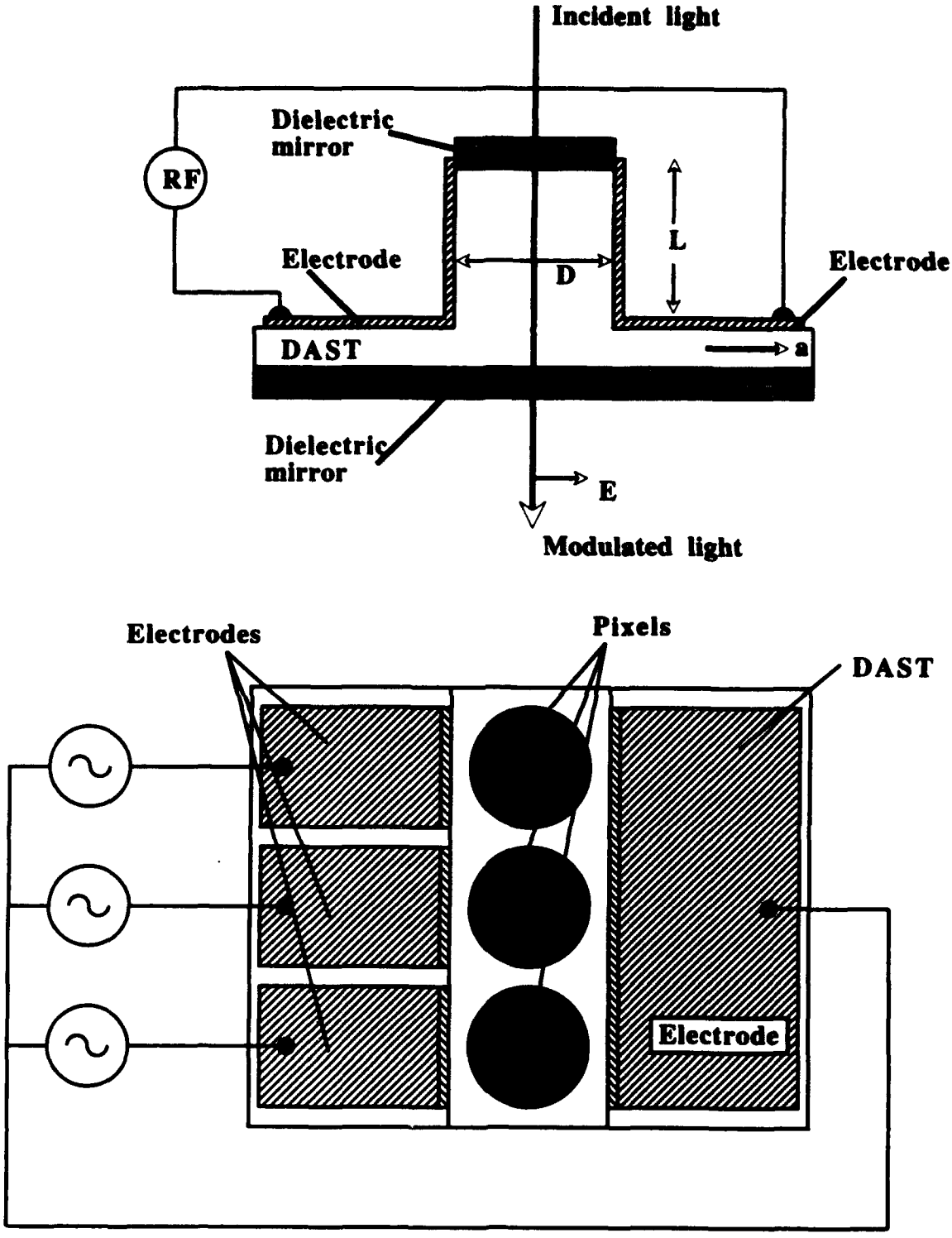

Figure 34: Architecture For A Fabry-Perot Optical Modulator.

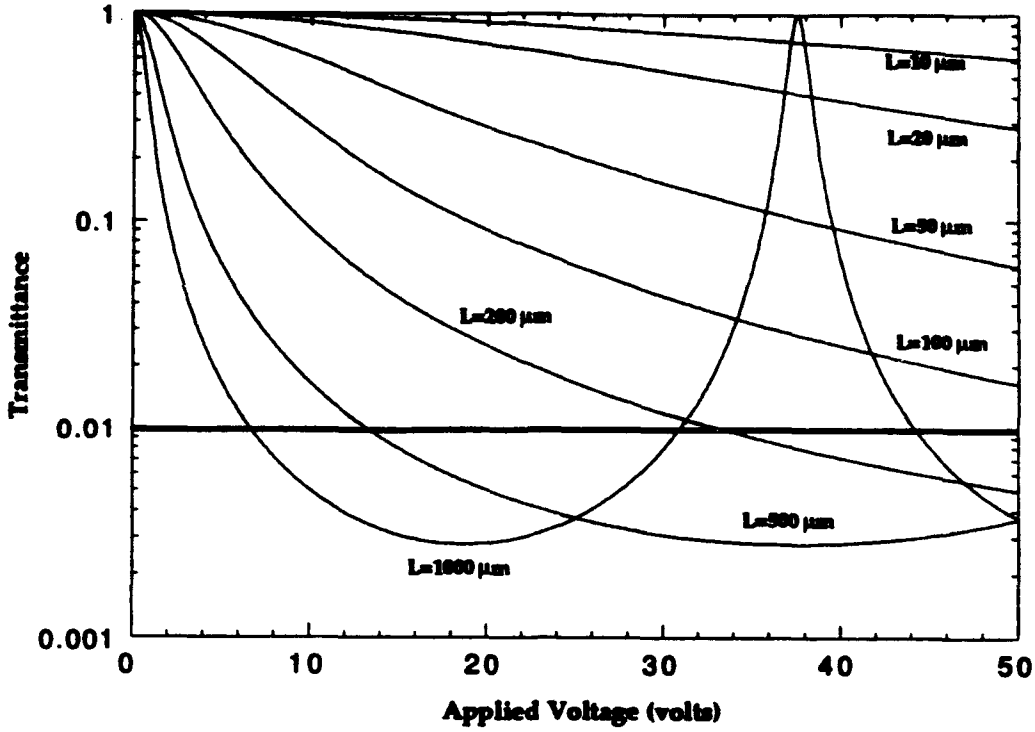

Figure 35: Transmittance versus Applied Voltage In Fabry-Perot Optical Modulator For 90% Reflective Mirrors.

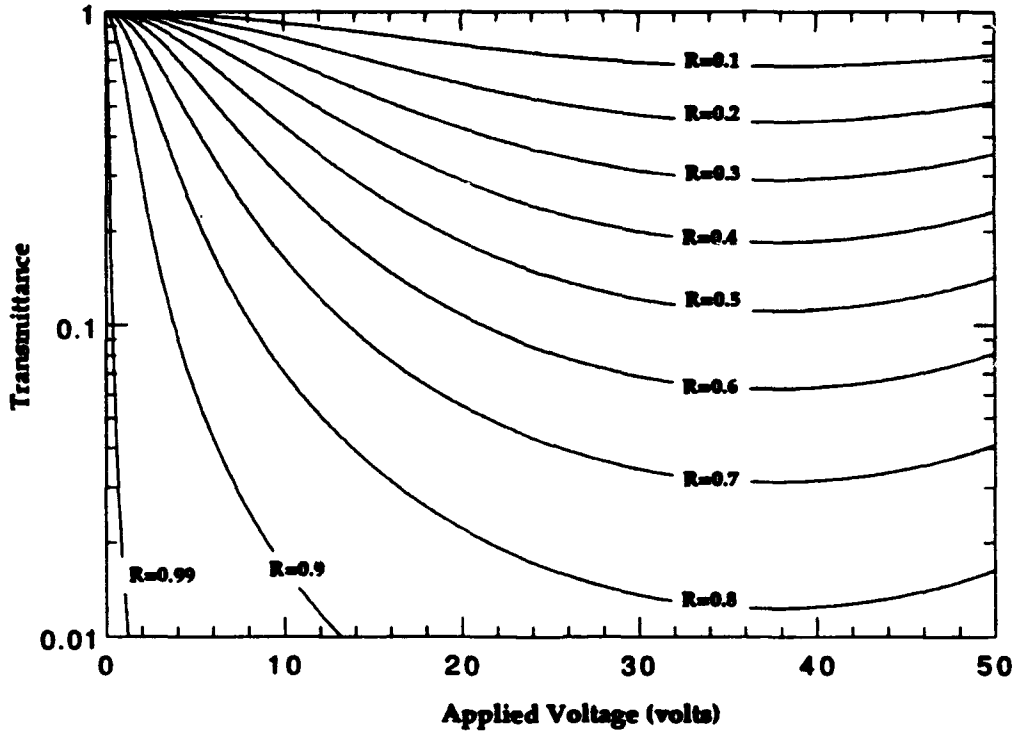

Figure 36: Transmittance versus Applied Voltage In Fabry-Perot Optical Modulator With 5:1 Aspect Ratio.

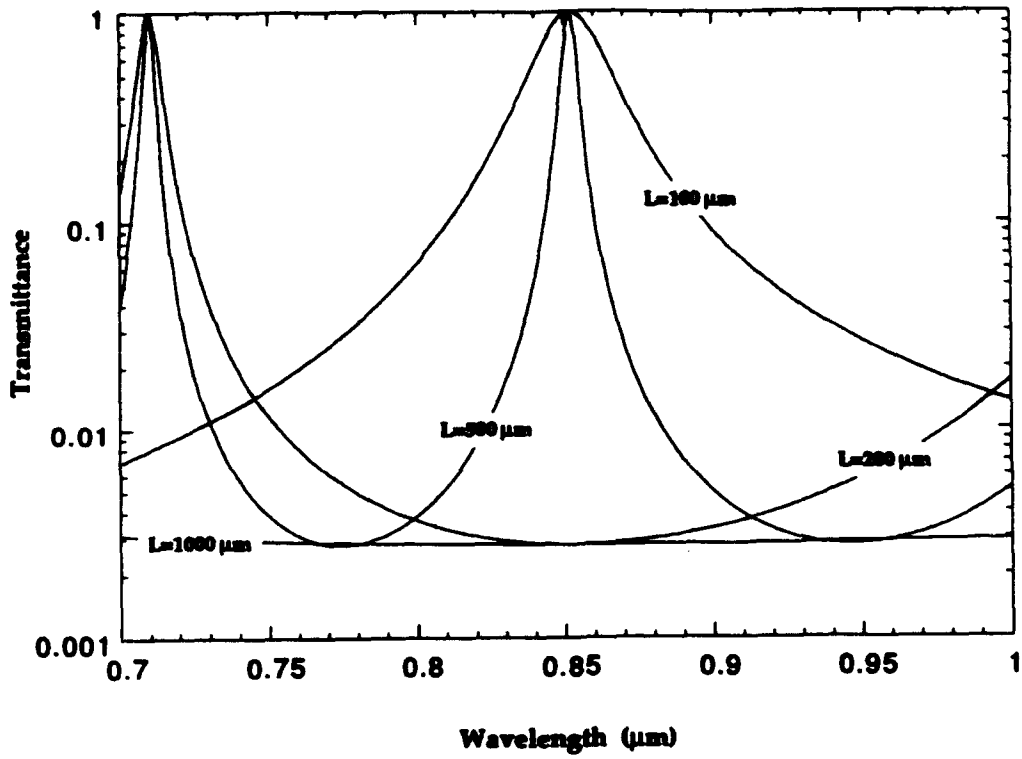

Figure 37: Wavelength Dependence of Fabry-Perot Optical Modulator

As a comparison, the response of a longitudinal modulator was also plotted, where the applied voltage is in a direction parallel to the path of propagation. In this case, the electrodes and dielectric mirrors are on the same surfaces, so that the aspect ratio is limited to 1:1. Also, since the orientation of the DAST *a*-axis relative to the optical polarization and the applied field must be compromised at 45°, the effective Pockels coefficient is reduced to $r_{11} = 50$ pm/V. The resulting curves in **Figure 38** show that a higher reflectance of R=0.99 is required to achieve high contrast switching in this geometry. The advantage of this approach is that, since the aspect ratio is fixed, the cavity length can be made arbitrarily short, increasing the free spectral range of the cavity and reducing its sensitivity to input wavelength variations.

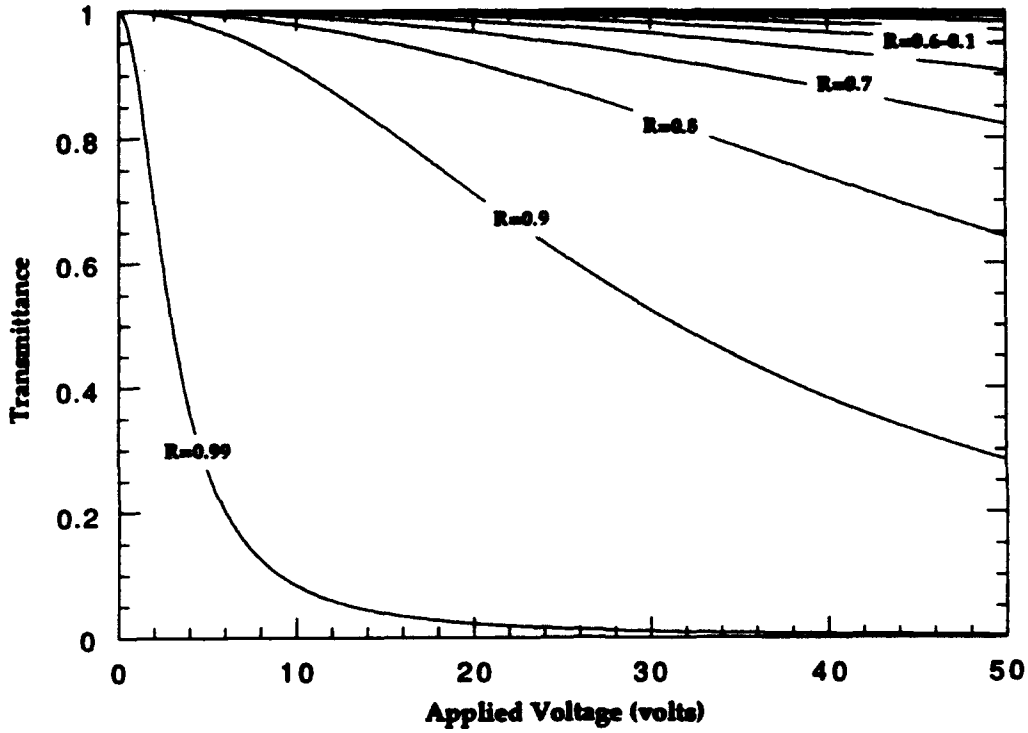

Figure 38: Transmittance versus Applied Voltage In Fabry-Perot Optical Modulator With 1:1 Aspect Ratio.

Fabrication Process:

As illustrated in **Figure 39**, an eximer laser photoablative technique has been used to machine structures in DAST crystals. Preliminary modulator structures were machined from DAST single crystal platelets mounted onto quartz substrates. The DAST crystal was planarized with a high-temperature epoxy to eliminate deleterious masking shadows and provided trenches for subsequent metallized contact pads. In this way, a single mask created a self-aligned electroded modulator array.

Several sets of modulators have been fabricated using an excimer laser processing technique to form the required structures in the DAST material. The excimer laser with an output per pulse of 30-40 mJ is focused using a cylindrical lens to a line approximately 250 μm wide and 2 cm long. The corresponding pulse energy density is on the order of 600-800 mJ / cm^2 . During ablation of the DAST material, the DAST surface was covered with the mask shown in **Figure 40**. The mask was mounted in an aluminum fixture to maintain good contact between the DAST surface and the metallic mask. During ablation a stream of helium gas was passed over the surface of the DAST and mask to minimize deposition of carbon by-products generated during the ablation process. The mask holder was mounted on a linear translation stage which translated the aperture of the mask at a velocity of ~ 1 mm / second, while the pulse repetition rate was maintained at ~ 10-20 Hz. The average removal rate for these parameters was 0.3-0.5 μm / pulse within the area of the focused laser

pulse. To remove approximately 100-200 μm of material and form the required trenches, the beam was pulsed across the sample surface over a period of 45-50 minutes. Although the ablation rate was slow, the quality of the sidewalls and trenches formed was excellent.

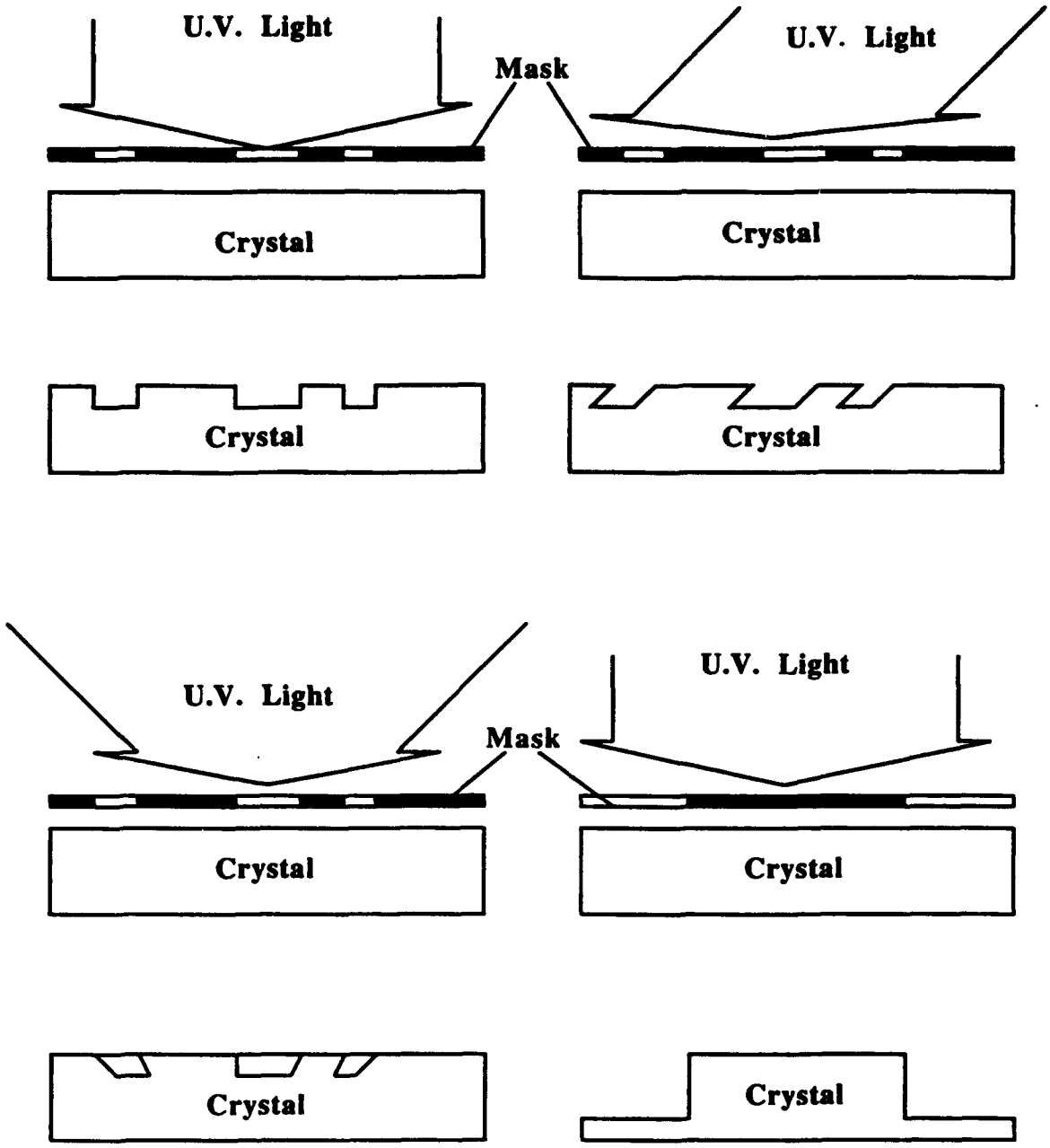

Figure 39: Eximer Laser Ablation Process for Fabry Perot Etalon Fabrication

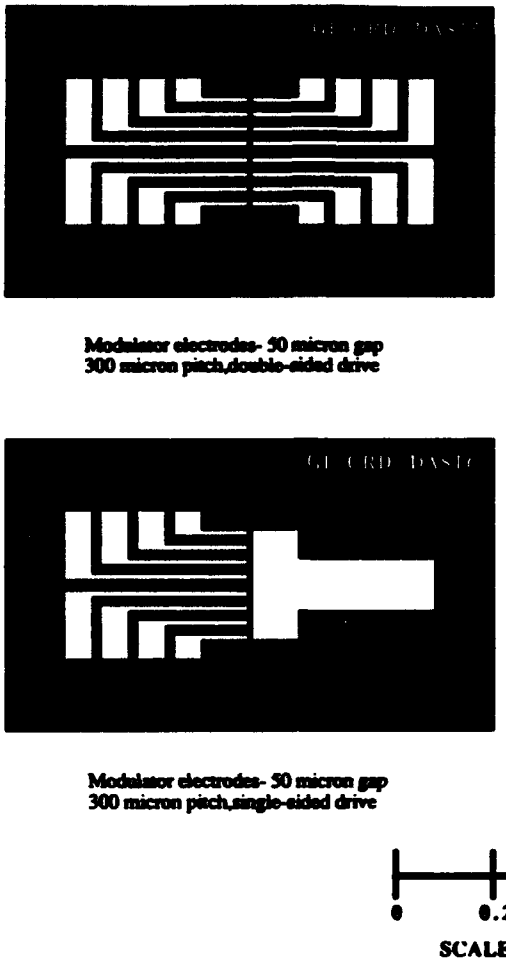

Figure 40: Shadow Masks Used For Fabry-Perot Fabrication.

Photomicrographs of several patterned structures are shown in **Figure 41.** Trenches 100 μm wide and up to 1000 μm deep were ablated into DAST crystals, giving structures with 10:1 aspect ratios. After machining, samples were mounted in conventional metallization equipment for deposition of electrodes. Since the trenches are aligned to the metal mask openings, the deposition of metal will be self-aligned to the trenches. Both sputtered and evaporated coatings of Au, Ag and Cr/Au or Cr/Ag were used. The best results were achieved using 300-500 Å of Cr followed by 1-2 μm of Au. Ag caused serious electrode migration problems during the high temperature life tests in air. During the evaporation, it was important to locate the sample directly over the evaporation source, and above it (at least 12-15 inches) to minimize thermal heating of the samples during deposition and to insure uniform coverage of the

trench sidewalls. Since the sidewalls angled inwards at 5-6°, the coating was usually excellent. Sputtered films had improved adhesion to the DAST surface, but invariably resulted in dirty coatings due to sputtering of DAST and mask material during the deposition. Sputtering also results in spillover of the metal coatings under the metal mask, shorting out the modulation sections to each other.

Figure 41: SEM Photograph of Eight Element Optical Modulator.

After metallization, the mask was removed and wire bonds or silver paint were used to make contact to the individual electrodes. Complete Fabry-Perot etalon modulators can then be assembled by sandwiching the structure between two etalon mirrors, having the desired reflectivity, or by depositing dielectric stacks directly onto the crystal faces.

Conclusions:

During the course of the investigations described in this report, we have determined that organic salts are very useful materials for optical device fabrication. It has been shown that DAST, and other related organic salts, can be designed and synthesized with improved electro-optic coefficients, along with useful dielectric constants, refractive indices, and optical windows of utility. These materials can be synthesized on large scale and crystals having useful device dimensions can be fabricated. It is still somewhat limiting that crystals of the materials are best grown from solution and that cutting and polishing of the crystals needs to be carried out to fabricate useful devices. While this is not impossible, it would be a dramatic improvement in the utility of the organic salts if a more suitable thin film deposition method were developed.

Optical modulators have been fabricated from DAST which have been demonstrated to have single pixel performance of greater that 1 GHz with contrast ratio of greater than 100:1, and required drive voltages less that 100 volts. Because of its outstanding physical stability for an organic compound, it has been demonstrated the DAST can be machined via laser ablation into useful device architectures for improved device performance. Because of the thermal stability of DAST, it is possible to vapor deposit electrode materials directly onto the crystal surfaces during device fabrication and its has even been demonstrated that the vapor pressure of DAST is sufficiently low as to allow its presence inside hermetically sealed laser diode packages without detrimentally affecting the performance of the laser.

The performance of DAST and other organic salts for electro-optic dives applications warrants further investigations. DAST has been demonstrated to have useful electro-optic performance to above 40 GHz, with indications that some applications above 1 THz are possible.

References:

1. "Stilbazolium Salt And Optically Non-Linear Devices Incorporating Same", E.P. Boden, P.D. Phelps, C.P. Yakymyshyn and K.R. Stewart, U.S. Patent #5,194,984 (1993).

2. "Process For The Preparation Of Stilbazolium Salts ", E.P. Boden, P.D. Phelps, and K.R. Stewart, U.S. Patent allowed.

3. "Optical Waveguides Comprising Deuterated Compounds," K.R. Stewart, E.P. Boden, and C.P. Yakymyshyn, U.S. Patent #5,323,482 (1994).

4. "Deuterated Organic Salts Useful In Nonlinear Optical Applications", K.R. Stewart, E.P. Boden and C.P. Yakymyshyn, U.S. Patent allowed .

5. "Optical Waveguides And Method For Their Fabrication", C.P. Yakymyshyn, E.P. Boden, P.D. Phelps and K.R. Stewart, U.S. Patent #5,094,553, (1992).

6. "High Melting Point Stilbazolium Salts", K.R. Stewart, U.S. Patent #5,292,888 (1994).

7. "High Resolution Micromachining of Organic Crystals And Optical Modulators Formed Thereby," C. P. Yakymyshyn, Y. S. Liu and R. Guida, U.S. Patent filed June 18, 1993.

8. 'Electro-Optic Sensor", C.P. Yakymyshyn, U.S. Patent filed June 18, 1993.

9. "Structure of Hydrated 4-Dimethylamino-N-methylstilbazolium Tosylate," G.L. Bryant, C.P. Yakymyshyn, and K.R. Stewart, *Acta Cryst., C49*, 350 (1993).

10. "Terahertz Optical Rectification from a Nonlinear Organic Crystal," X.-C. Zhang, X.F. Ma, Y. Jin, T.-M. Lu, E.P. Boden, P.D. Phelps, K.R. Stewart and C.P. Yakymyshyn, *Applied Physics Letters, 61*(26), 3080 (1993).

11. "Organic Crystals Give Optoelectronics a Boost," K.R. Stewart, *Photonics Spectra*, 104, July 1994 (invited article).

12. "Scaling of Terahertz Optical Rectification from Nonlinear Crystals," T.J. Carrig, G. Rodriguez, T.S. Clement, A.J. Taylor and K.R. Stewart, submitted to *Applied Physics Letters* (1994).

13. "Generation of Terahertz Radiation Using Electro-Optic Crystal Mosaics," T.J. Carrig, G. Rodriguez, T.S. Clement, A.J. Taylor and K.R. Stewart, submitted to *Applied Physics Letters* (1994).